Structure

Article

Mechanism of SHP2 activation by bis-Tyr-phosphorylated Gab1

Graphical abstract

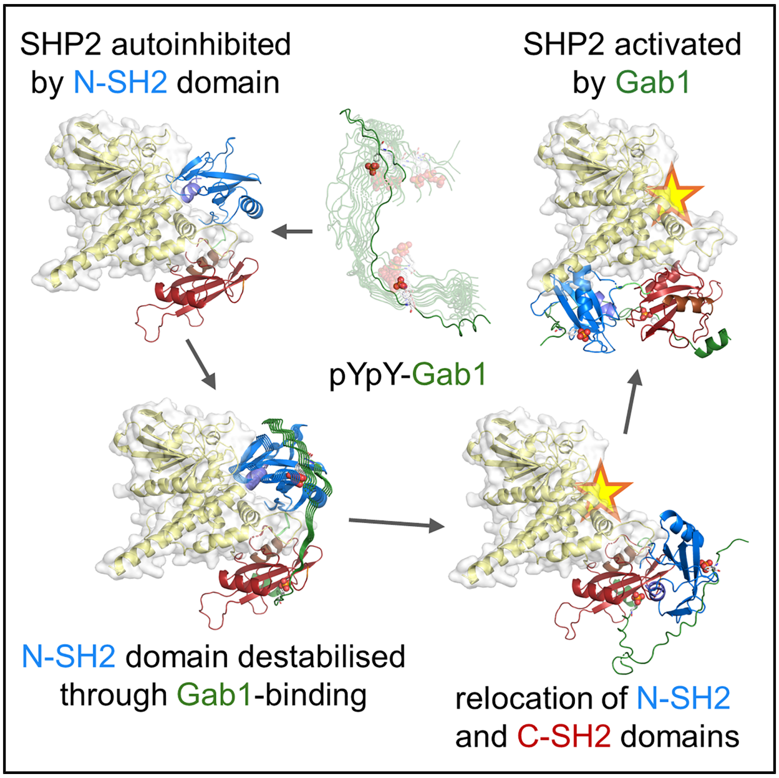

Authors

Lisa Machner, Alaa Shaikhqasem,
Tobias Gruber, ...,
Panagiotis L. Kastritis,
Stephan M. Feller, Milton T. Stubbs

Correspondence

stephan.feller@uk-halle.de (S.M.F.),
stubbs@biochemtech.uni-halle.de (M.T.S.)

In brief

The SH2 domain-containing tyrosine phosphatase SHP2 is autoinhibited in the absence of ligands. Combining calorimetry and NMR spectroscopy as well as X-ray and electron crystallography, Machner et al. propose a two-state model for the activation of SHP2 by an intrinsically disordered bis-phosphorylated Gab1 peptide.

Highlights

- bis-phosphorylated Gab1 peptide binds to SHP2 SH2 domains and alters their dynamics
- Intrinsically disordered Gab1 peptide adopts secondary structure upon SHP2 binding
- SHP2 tandem SH2 domains display a compact conformation upon Gab1 peptide binding
- Model presented for SHP2 autoinhibition release by intrinsically disordered peptide

Machner et al., 2026, Structure *34*, 1–13
March 5, 2026 © 2025 The Authors. Published by Elsevier Inc.
https://doi.org/10.1016/j.str.2025.11.018

Please cite this article in press as: Machner et al., Mechanism of SHP2 activation by bis-Tyr-phosphorylated Gab1, Structure (2025), https://doi.org/10.1016/j.str.2025.11.018

Structure

CellPress
OPEN ACCESS

Article

Mechanism of SHP2 activation by bis-Tyr-phosphorylated Gab1

Lisa Machner,[1,2,5] Alaa Shaikhqasem,[1,5,8] Tobias Gruber,[2,3,5,8] Farzad Hamdi,[1,4,8] Constanze Breithaupt,[1,5] Judith Kniest,[1,2,5] Felix Wiebe,[1,2,5] Marc Lewitzky,[2,5] Christoph Parthier,[1,5] Fotis L. Kyrilis,[1,4,6] Jochen Balbach,[3,4,7] Panagiotis L. Kastritis,[1,4,6,7] Stephan M. Feller,[2,5,*] and Milton T. Stubbs[1,4,5,7,9,*]

[1]Institut für Biochemie und Biotechnologie, Martin-Luther-Universität Halle-Wittenberg, 06120 Halle (Saale), Germany
[2]Institut für Molekulare Medizin, Martin-Luther-Universität Halle-Wittenberg, 06120 Halle (Saale), Germany
[3]Institut für Physik, Martin-Luther-Universität Halle-Wittenberg, 06120 Halle (Saale), Germany
[4]ZIK HALOmem, Biozentrum, Martin-Luther-Universität Halle-Wittenberg, 06120 Halle (Saale), Germany
[5]Charles-Tanford-Proteinzentrum, Martin-Luther-Universität Halle-Wittenberg, 06120 Halle (Saale), Germany
[6]Institute of Chemical Biology, National Hellenic Research Foundation, 11635 Athens, Greece
[7]Mitteldeutsches Zentrum für Struktur und Dynamik der Proteine, Martin-Luther-Universität Halle-Wittenberg, 06120 Halle (Saale), Germany
[8]These authors contributed equally
[9]Lead contact
*Correspondence: stephan.feller@uk-halle.de (S.M.F.), stubbs@biochemtech.uni-halle.de (M.T.S.)
https://doi.org/10.1016/j.str.2025.11.018

SUMMARY

The non-receptor tyrosine phosphatase SHP2 (SH2 domain-containing protein tyrosine phosphatase 2) (PTPN11) is a regulator of diverse cellular functions including mitogenic activation and cell migration. It comprises two tandem Src-homology 2 (SH2) domains followed by the catalytic domain and is autoinhibited by the N-terminal SH2 domain blocking access to the active site. Mutations influencing auto-inhibition have been implicated in cancer and other diseases, and allosteric inhibitors have been developed that stabilize the inactive state. Here, we show that the intrinsically disordered bis-phosphorylated SHP2-activating peptide pY^{627}pY^{659}-Gab1 binds to both SH2 domains, undergoing partial ordering in the process. In addition to eliciting changes in SH2 domain dynamics, the peptide reorganizes their relative orientations to generate a new SH2-SH2 interface. Our data suggest an active conformation for SHP2 that is also applicable to the hematopoietic cell-specific SHP1 (PTPN6), shedding light on the activation mechanism of both enzymes and paving the way for the development of novel compounds to modulate SHP2 activity.

INTRODUCTION

The Src-homology 2 (SH2) domain-containing protein tyrosine phosphatase 2 (SHP2 or PTPN11) is an important regulator of cellular processes through the Ras/MAP kinase signaling pathway, which has been implicated in a number of cancers[1] and is upregulated in diabetes.[2] The enzyme consists of two N-terminal tandem SH2 domains (N-SH2 and C-SH2) that bind phosphorylated tyrosine (pY) residues of binding partners, followed by a protein tyrosine phosphatase (PTP) domain and an intrinsically disordered C-terminal region (Figure 1). In the absence of pY-bearing partners, the N-SH2 domain binds to the PTP catalytic site, blocking substrate access and maintaining SHP2 in an autoinhibited or “closed” state[4] (Figure 1B). The crystal structure of the constitutively active oncogenic mutant SHP2^{E76K}[5] reveals an open active site, with the C-SH2 domain rotated by ca. 120° with respect to the PTP domain and the N-SH2 relocated to the opposite face (Figure 1C). This rearrangement can be reversed in the presence of the allosteric inhibitor SHP099[6] to stabilize the autoinhibited state.[5,7]

The importance of tightly regulated SHP2 activity is evident in several genetic disorders. Fifty percent of patients with Noonan syndrome (NS) and 90% of patients with NS with multiple lentigines (NSML, formerly LEOPARD syndrome) harbor germline mutations in SHP2,[8,9] many of which exhibit increased basal activity.[10] Both NS and NSML may predispose patients to juvenile myelomonocytic leukemia, an aggressive leukemia of infants and children, and SHP2 activation by the bacterial effector protein CagA from *Helicobacter pylori* (*Hp*CagA) has been implicated in gastric carcinogenesis.[11,12] On the other hand, SHP2 has been demonstrated to act as a tumor suppressor in some liver and colorectal cancers,[13,14] possibly due to SHP2-dependent dephosphorylation of the STAT family transcription factor STAT5A.[15]

SHP2 is activated by pY-peptides binding to the SH2 domains, which is thought to elicit conformational changes in the enzyme.[16] Some activators are high-affinity binding partners that interact solely with the N-SH2 domain,[17,18] whereas a number of SHP2 activators possess tandem tyrosine phosphorylation sites.[19,20] Studies on the interaction of the N-SH2-C-SH2

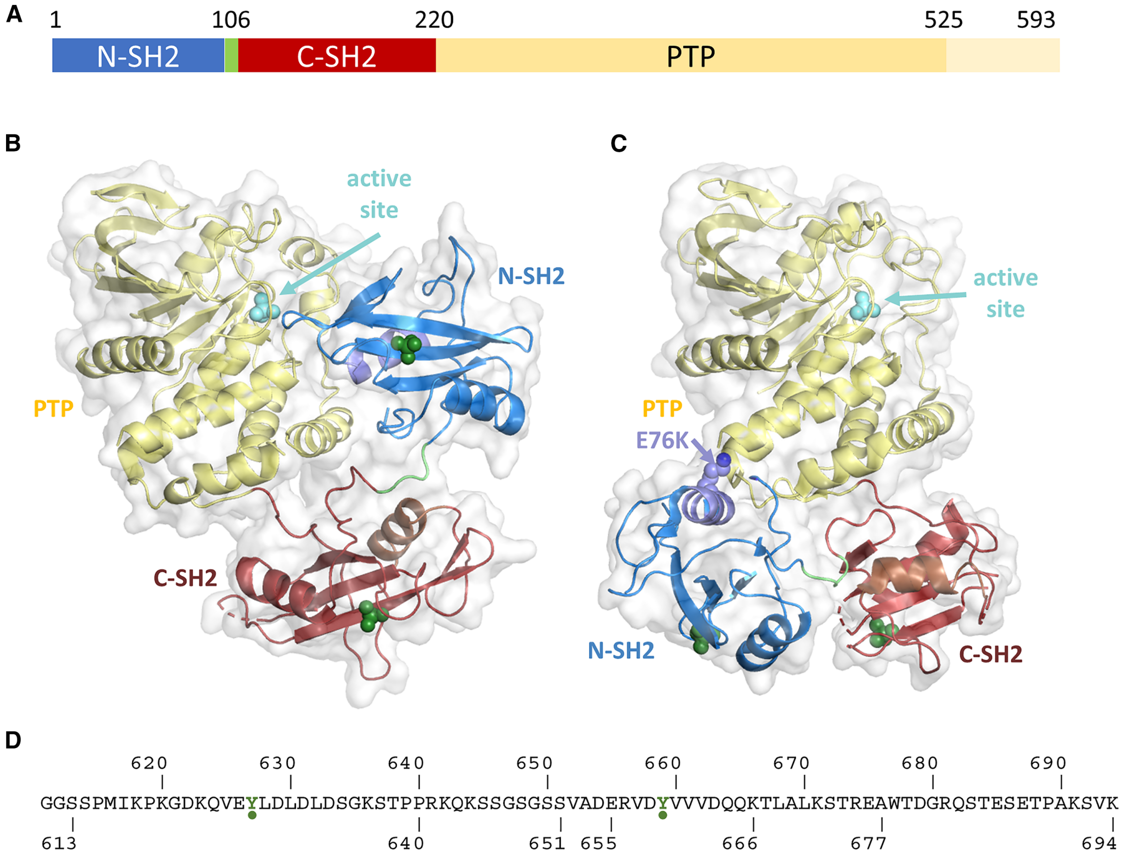

Figure 1. SHP2 structural elements

(A) Domain organization of SHP2 (human residue numbering), consisting of two SH2 domains (blue and red) joined by a short linker (green) followed by the PTP catalytic domain (yellow). The latter possesses an intrinsically disordered C-terminal extension that harbors both serine and tyrosine phosphorylation sites[3]; the extension can be dispensed with for activity measurements and is truncated in SHP2 structures.

(B) Crystal structure of SHP2 in its autoinhibited state[4] (pdb code 2shp). The N-terminal SH2 domain blocks access to the PTP active site, marked by cyan spheres showing the phosphate position of phosphotyrosine (pY) substrates. To aid orientation, locations of the SH2 pY phosphate-binding sites are marked by green spheres and SH2 αB helices (see Figure 3) are in separate tones (αB^{N-SH2}, light violet; αB^{N-SH2}, brown).

(C) The constitutively active oncogenic $SHP2^{E76K}$ mutation E76K results in a substantial reorganization of the N- and C-SH2 domains[5] (pdb 6crf), unmasking the active site for substrate dephosphorylation. Orientation of the PTP domain as in (B).

(D) Sequence of $Gab1^{611-694}$, with (p)Y residues $(p)Y^{627}$ and $(p)Y^{659}$ marked in green.

tandem domain from SHP2 with bis-phosphorylated pYpY-peptides from *Hp*CagA[17] and from the programmed cell death protein 1 (PD-1)[21] have shown that it is possible for the tandem domain to engage both pY moieties simultaneously. The latter study revealed conformational rearrangements in the tandem domain upon pYpY-PD-1 peptide binding, which is in keeping with an opening of the active site as the short 24-amino acid pYpY-PD-1 linker[21,22] is unable to span the N-SH2 and C-SH2 pY-binding sites in the autoinhibited closed SHP2 conformation.[4] On the other hand, the arrangement of the SH2 domains in the constitutively E76K active open conformation[5] is also incompatible with simultaneous binding of both pY moieties in PD-1, so that the mechanism whereby bis-phosphorylated peptides activate SHP2 remains unclear.

The Grb2-associated binding protein 1 (Gab1) is a hub protein composed of a folded pleckstrin homology (PH) domain that binds phosphatidylinositol lipids in the membrane and a 570-amino acid long disordered tail that serves as a docking site for SH2 and SH3 domain-containing binding partners.[23,24] Phosphorylation of the two tyrosines Y^{627} and Y^{659} near the Gab1 C terminus results in the binding and activation of SHP2.[25,26] We have previously shown that the Gab1 caspase cleavage C-terminal fragment G^{611}-K^{694}[27] (Figure 1D) is disordered in solution both in the unphosphorylated and bis-phosphorylated states, with residues C-terminal to $(p)Y^{659}$ exhibiting a slight helical propensity.[28] Here, we investigate the interaction between the bis-phosphorylated fragment $pY^{627}pY^{659}$-$Gab1^{613-694}$ and the N-SH2-C-SH2 tandem domain $SHP2^{1-222}$.

RESULTS

Binding of bis-phosphorylated $pY^{627}pY^{659}$-$Gab1^{613-694}$ to the $SHP2^{1-222}$ tandem domain was investigated initially using isothermal titration calorimetry (ITC), demonstrating an apparent K_d of 37 ± 13 nM that involves a strong enthalpic component (Figure 2A). Interactions with the isolated $N\text{-}SH2^{1-106}$ and

Please cite this article in press as: Machner et al., Mechanism of SHP2 activation by bis-Tyr-phosphorylated Gab1, Structure (2025), https://doi.org/10.1016/j.str.2025.11.018

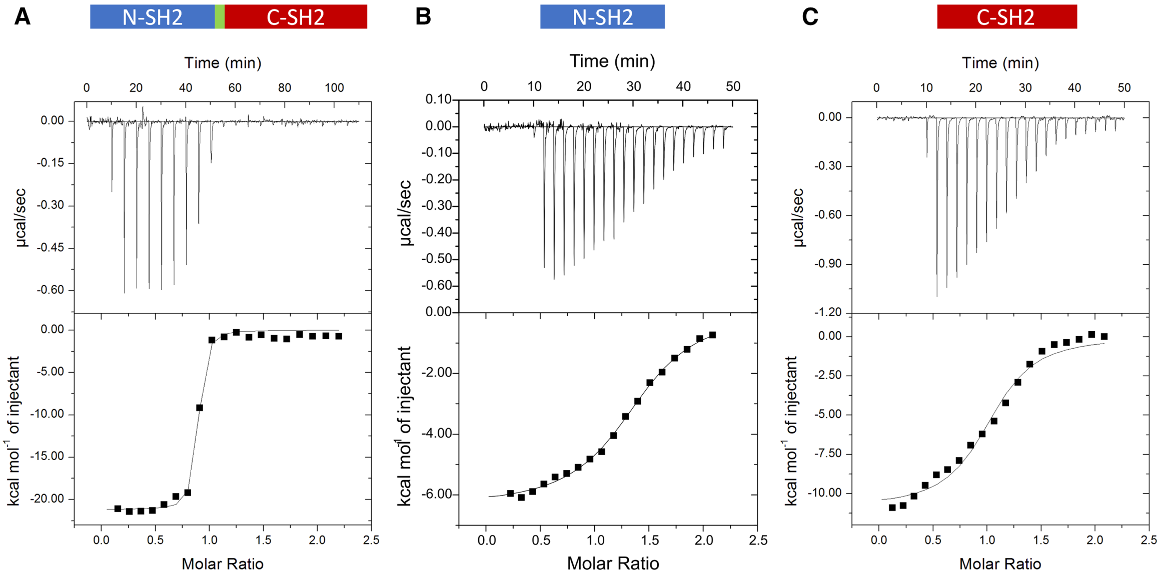

	$Shp2^{1-222}$: $Gab1^{613-694}$	$N\text{-}SH2^{1-106}$: $Gab1^{613-94}$	$C\text{-}SH2^{102-220}$: $Gab1^{613-94}$
N	0.98 ± 0.07	1.25 ± 0.08	1.14 ± 0.10
K_D [nM]	37 ± 13	3089 ± 1881	2712 ± 156
- ΔS · T [cal mol^{-1}]	9551 ± 478	-1508 ± 659	4085 ± 281
ΔH [cal mol^{-1}]	-19743 ± 273	-5924 ± 370	-11677 ± 193
ΔG [cal mol^{-1}]	-10144 ± 180	-7432 ± 316	-7592 ± 102

Figure 2. Analysis of binding of $pY^{627}pY^{659}$-$Gab1^{613–694}$ to SHP2 SH2 domains by ITC

(A) The tandem SH2 domain $SHP2^{1–222}$ binds with an apparent K_d of 37 nM with a strong enthalpic component.

(B and C) The same peptide binds the isolated domains $N\text{-}SH2^{1–106}$ and $C\text{-}SH2^{102–220}$ 100-fold weaker. See also Figure S1.

$C\text{-}SH2^{102–220}$ are approximately 2 orders of magnitude weaker (Figures 2B and 2C), with minor deviations from a 1:1 binding model apparent from the isotherms. Mutation of the two phosphotyrosine binding sites to yield the tandem variants $SHP2^{1–222}$-$C\text{-}SH2^{dead}$ ($R^{138}A/H^{169}A$) and $SHP2^{1–222}$-$N\text{-}SH2^{dead}$ ($R^{32}A/H^{53}A$),[17] which in the isolated domains abrogates binding, resulted in an expected decrease in affinity that was, nevertheless, higher than that for the isolated domains (Figures S1A–S1C). No interaction could be detected for the separate $N\text{-}SH2^{1–106}$ and $C\text{-}SH2^{102–220}$ domains with the singly phosphorylated peptides pY^{659}-$Gab1^{640–694}$ and pY^{627}-$Gab1^{613–651}$, respectively (Figures S1D and S1E), delineating the specificities of each domain.

The X-ray crystal structure of the N-SH2 domain $SHP2^{1–106}$ in complex with pY^{627}-$Gab1^{613–651}$ (Figures 3A and S2A; Table 1) reveals binding of phosphopeptide residues $pY^{627}Gab1^{624–632}$ (amino acids −3 to +5, numbered relative to pY^{627}) perpendicular to the central SH2 β-sheet in an extended (canonical) manner typical of SH2-peptide complexes,[29] with the side chains of V^{625}, L^{628}, L^{630}, and L^{632} occupying hydrophobic surfaces of the N-SH2 domain. The binding of $pY^{627}pY^{659}$-$Gab1^{613–694}$ to the isolated N-SH2 domain in solution was mapped using nuclear magnetic resonance (NMR) (Figures 4A and S3A). Titration of the ^{15}N,^{13}C-labeled phosphopeptide to the unlabeled $N\text{-}SH2^{1–106}$ domain (Figure S3A) yields chemical shift perturbations (CSPs) of residues adjacent to pY^{627} in agreement with the crystal structure, as do chemical shift indices (CSIs) that indicate an extended backbone conformation for Gab1 peptide residues 625–632. Dynamic relaxation and heteronuclear NOE (hNOE) data on the peptide (Figure S3C) indicate conformational restriction of residues K^{623}-K^{636} upon N-SH2 binding, whereas residues P^{640}-V^{660} remain disordered as in the free phosphopeptide.[28] Surprisingly, CSPs are also seen around pY^{659} in the presence of the N-SH2 domain, suggesting that the latter can bind both phosphotyrosine residues. Complementary experiments titrating the unlabeled $pY^{627}pY^{659}$-$Gab1^{613–694}$ peptide to the ^{15}N-labeled $N\text{-}SH2^{1–106}$ domain (Figures 4A and 4B) are also in agreement with the crystal structure. Interestingly, order parameters of ^{15}N-labeled $N\text{-}SH2^{1–106}$ in the presence and absence of pY^{627}-$Gab1^{613–651}$ (Figures S4A–S4C) derived from NMR relaxation experiments (Figure S5) indicate enhanced dynamics throughout most of the domain upon phosphopeptide binding, although residues of the αB helix and the BG-loop exhibit increased order parameters.

Although we were unable to obtain crystals of the C-SH2 domain, either in the presence or absence of peptides, the

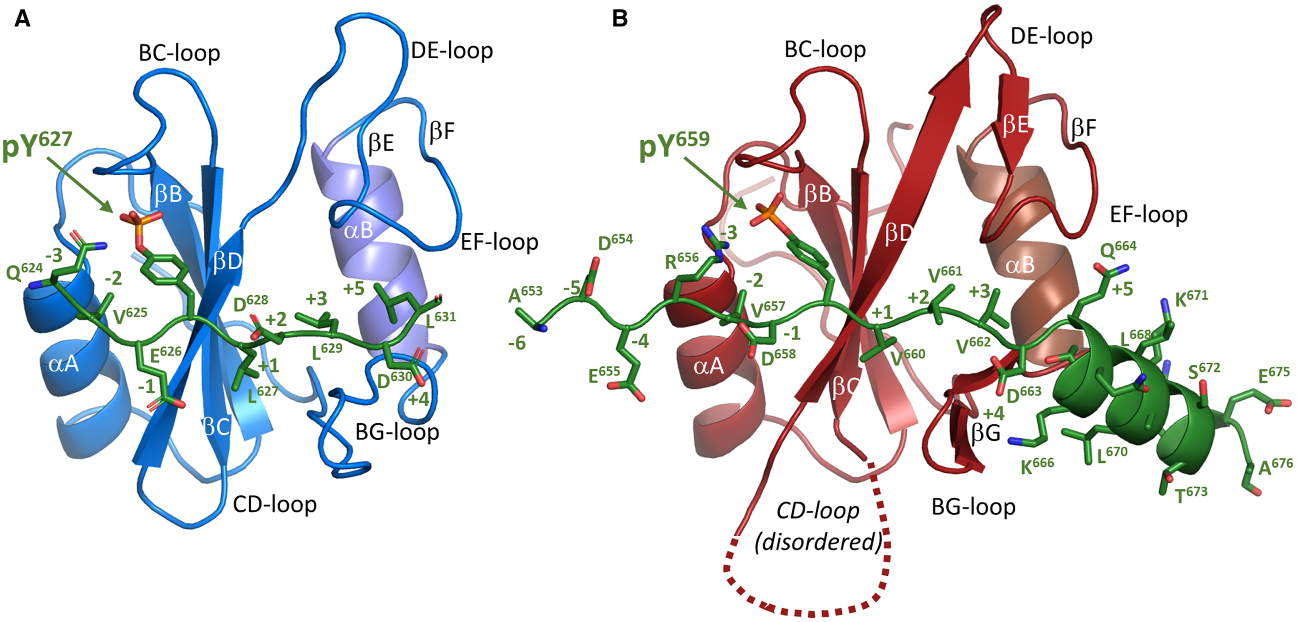

Figure 3. Phosphotyrosine peptide binding to SHP2 SH2 domains

(A) X-ray crystal structure of the N-SH2 domain bound to the pY^{627}-Gab1$^{613–651}$ peptide (green sticks). The phosphopeptide (residue numbering from −3 to +5 relative to pY^{627}) binds perpendicular to the central SH2 β-sheet in an extended manner.

(B) Binding mode of pY^{659}-Gab1$^{653–676}$ to the C-SH2 domain determined from the electron crystallographic structure determination of the N-SH2-C-SH2-tandem SHP2$^{1–222}$ construct in complex with pY^{627}pY^{659}-Gab1$^{617–684}$; C-SH2 oriented as in (A). Note the hydrophilic Gln side chain in position pY^{659} + 5 and the presence of the C-terminal helix Q^{664}-A^{676}. See also Figure S2.

N-SH2-C-SH2-tandem SHP2$^{1–222}$ construct in complex with pY^{627}pY^{659}-Gab1$^{617–684}$ yielded thin needle-like crystals with multiple lattices that proved unsuitable for X-ray crystallography. Using 3D electron diffraction,[30–32] however, orthorhombic microcrystals of the complex could be analyzed to yield a structure to 3.2 Å resolution (Table 1). Interpretable Coulomb potential density (Figure S2B) is observed for the tandem SH2 domain from W^{6} to I^{221} (with a break between T^{153} and K^{164}, i.e., C-SH2 loop CD, in agreement with in-solution NMR relaxation analyses that indicate high local dynamics—order parameters $S^2 < 0.5$ in both the free and peptide bound states—of C-SH2 residues D^{162}-S^{165} [Figure S4D]) and for the Gab1 peptide from Q^{624} to A^{676}, with disordered linker residues G^{635}-V^{652} (Figures S2B–S2F). Due to the disorder of the peptide linker, it is not possible to differentiate between the binding of a single pYpY-peptide to one tandem N-SH2 C-SH2 domain, two separate peptides binding to each domain, or one pYpY-peptide linking symmetry-related tandem domains in the crystal (Figure S6). As in the crystal the shortest possible Cα-Cα distance of 28 Å between S^{634} and A^{653} corresponds to the binding of both pY^{627}-Gab1 and pY^{659}-Gab1 peptide segments to the SH2 domains of a single tandem domain, a 1:1 binding mode represents the most likely scenario. Gab1 residues pY^{627}Gab1$^{622–631}$ bind to the N-SH2 domain in the canonical manner observed in the single-domain structure (Figures S2A and S2C). In contrast, the 24-residue segment pY^{659}-Gab1$^{653–676}$ binds the C-SH2 domain in a bipartite manner (Figures 3B and S2D), with amino acids −6 to +3 (A^{653} to V^{662}) in an extended conformation and residues +4 to +17 (D^{663} to A^{676}) forming an α-helix. The helix not only affords a larger binding interface between the C-terminal peptide and C-SH2 but also the canonical hydrophobic interaction between residue pY+5 (in this case Q^{664}, whose side chain is disordered) with a hydrophobic patch of the SH2 domain is replaced by similar interactions with the side chains of T^{667} and L^{670} (formally residues +8 and +11). Superposition of the N- and C-SH2 domains reveals distinct backbone conformations of the EF loop (^{65}LYGGE^{69} vs. ^{181}VGGGE^{185}), which might relax the specificity for hydrophobic pY+5 residues in the C-SH2 domain, as well as in the BG-loop (^{84}HHGQL^{88} vs. ^{200}NPM^{202}), which facilitates accommodation of the C-terminal helix in the C-SH2 domain (Figure S7). These features of the N- and C-SH2 domains are conserved absolutely in SHP2 and partially in SHP1 sequences (Figure S8).

ITC experiments provide support for the unusual mode of binding to the C-SH2 domain (Figure 5). Titration of the monophosphorylated Gab1 peptide pY^{659}-Gab1$^{655–677}$ to C-SH2$^{102–220}$ (Figure 5B) yields an apparent affinity of 4 μM, comparable to that of the bis-phosphorylated pY^{627}pY^{659}-Gab1$^{613–694}$ (Figure 2C), whereas C-terminal truncation (pY^{659}-Gab1$^{655–666}$) results in a 10-fold reduction (Figure 5C) and the corresponding C-terminal peptide Gab1$^{667–677}$ elicits no change in enthalpy (Figure 5D). NMR CSPs of the isotope labeled bis-phosphorylated peptide in the presence of the C-SH2 domain (Figure S3B) agree with an extensive binding site around pY^{659}, comprising Gab1 residues E^{655}-K^{671}. The binding site is divided into two regions, with CSIs indicating residues V^{661}-Q^{665} to be in an extended and residues A^{669}-T^{673} in a helical conformation. Corresponding data for the labeled C-SH2$^{102–220}$ domain with pY^{659}-Gab1$^{655–677}$ and the C-terminally truncated peptide pY^{659}-Gab1$^{655–666}$ (Figures 4C–4F) also support the binding mode observed in the pY^{627}pY^{659}-Gab1$^{613–694}$ peptide: N-SH2-C-SH2-tandem SHP2$^{1–222}$ domain

Please cite this article in press as: Machner et al., Mechanism of SHP2 activation by bis-Tyr-phosphorylated Gab1, Structure (2025), https://doi.org/10.1016/j.str.2025.11.018

Table 1. X-ray crystallographic and MicroED data collection and refinement statistics for the complexes

	N-SH2$^{1–106}$ domain/ pY^{627}-Gab1$^{613–651}$	SHP2$^{1–222}$ tandem domain/ pY^{627}pY^{659}-Gab1$^{617–684}$
pdb code	9qa5	9qcd
Diffraction data		
Radiation source	X-ray rotating anode (CuKα)	Electron microscope (excitation voltage 200 kV)
Wavelength (Å)	1.5406	0.025
# crystals used	1	2
d_{min} (Å)	69.85–2.08 (2.14–2.08)[a]	33.7–3.20 (3.39–3.20)
Space group	$P4_32_12$	$P2_12_12_1$
a, b, c (Å)	60.78, 60.78, 69.85	30.59, 82.25, 117.76
Observations	118,443 (8,416)	56,190 (9.163)
Unique reflections	8,364 (633)	4,729 (744)
Multiplicity	14.2 (13.3)	11.9 (12.3)
Completeness	100% (100%)	88.8% (89.7%)
$CC_{1/2}$	99.8% (81.7%)	94% (53%)
R_{meas}	13.7% (95.0%)	80.2% (220%)
$<I/\sigma(I)>$	14.0 (2.9)	3.29 (1.41)
Mosaicity	0.29°	–
Solvent content (%)	38.3	58.5
Wilson B-factor (Å^2)	28.4	47.2
Refinement		
Reflections (# work/free)	7,890/405	4,487/238
Data range (Å)	27.87–2.08	33.72–3.20
Rwork/Rfree (%)	22.6/27.3	30.1/35.3
Non-hydrogen atoms (#)	921	1,932
Protein	797	1,642
Peptide	81	290
Solvent	43	0
Amino acids	108	241
Protein	99	206
Peptide	9	35
RMS_{bonds} (Å)	0.006	0.003
RMS_{angles} (°)	0.95	0.648
Ramachandran (%)		
Favored	96.0	95.6
Allowed	4.0	4.4
Outlier	0.0	0.0
Average B-factor ()		
Protein	34.64	48.96
Peptide	51.55	65.95
Solvent	36.15	–

[a] Values in parentheses correspond to the highest resolution shell.

complex crystal. Compared to the N-SH2 domain, changes in the dynamics of the C-SH2 domain are more localized upon Gab1 peptide binding (Figures S4D–S4F), with residues 175–200 in particular becoming more dynamic.

The pYpY-Gab1-peptide-bound tandem domain exhibits a compact arrangement (Figure 6A), with C-SH2 P^{144} nestling in a hydrophobic pocket formed by the N-SH2 residues W^{6}, F^{7}, F^{41}, Y^{63}, and L^{74} (Figure 6B). In structures of autoinhibited SHP2, this pocket is partially occupied by the side chain of R^{4}, and access is restricted by residues from the catalytic domain (Figure S9C). The two domains exhibit variable and more extended arrangements, with little or no interdomain contacts, in N-SH2-C-SH2-PTP SHP2 wild-type and E76K variant structures (Figures 6C and 6D), as well as in structures of SHP2 tandem SH2 domains in the presence of short monophosphorylated peptides (Figures 6E–6G), indicating the N- and C-SH2 domains

Please cite this article in press as: Machner et al., Mechanism of SHP2 activation by bis-Tyr-phosphorylated Gab1, Structure (2025), https://doi.org/10.1016/j.str.2025.11.018

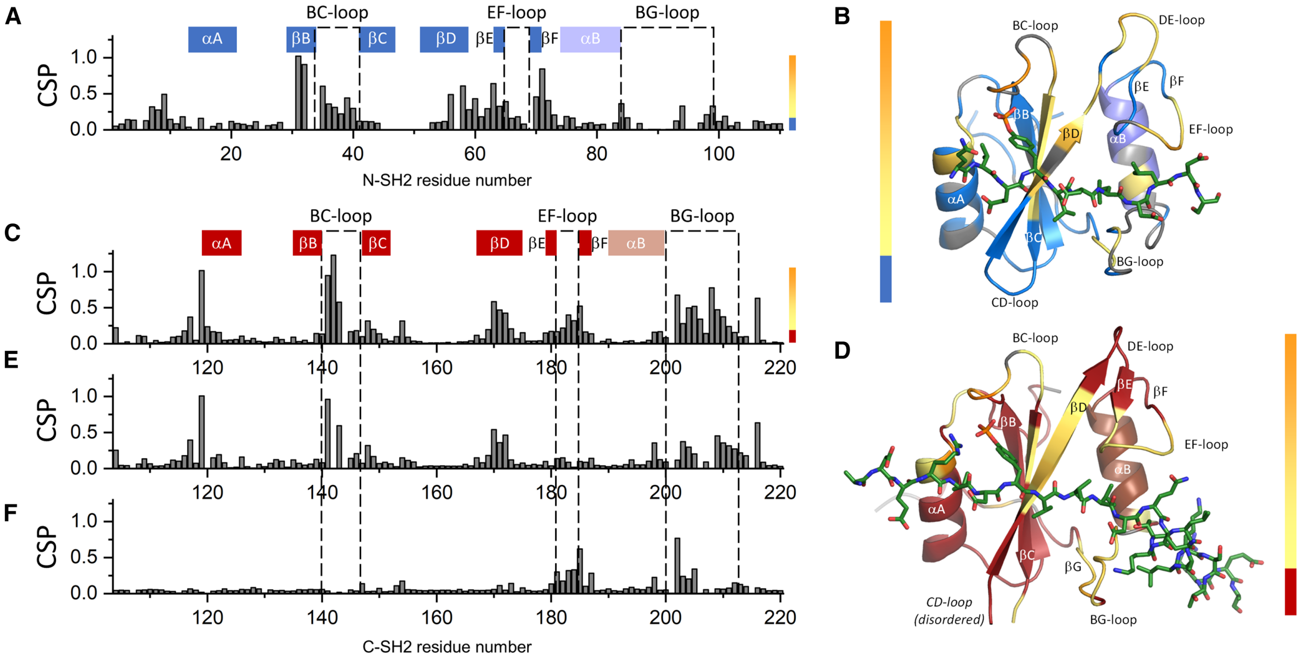

Figure 4. Mapping the binding of $pY^{627}pY^{659}$-$Gab1^{613–694}$ to N-$SH2^{1–106}$ and C-$SH2^{106–220}$ in solution

(A and B) (A) CSPs in ppm of ^{15}N-N-$SH2^{1–106}$ upon titration of unlabeled $pY^{627}pY^{659}$-$Gab1^{613–694}$ plotted against residue number. Mapping these to the crystal structure (B) shows that they are in agreement with the X-ray crystal structure, with CSPs above the mean value color-ramped from the mean (pale yellow) to the maximum (orange) values; non-assigned residues colored gray.

(C and D) Corresponding CSPs of ^{15}N-C-$SH2^{106–220}$ upon binding of pY^{659}-$Gab1^{655–677}$ are also in agreement with the crystal structure.

(E and F) (E) C-terminal truncation of the peptide to pY^{659}-$Gab1^{655–666}$ results in reduced shifts for residues of the C-SH2 domain EF and BG loops, i.e., residues that contact the C-terminal helix. CSPs comparing ^{15}N-C-$SH2^{106–220}$ bound to pY^{659}-$Gab1^{655–677}$ and pY^{659}-$Gab1^{655–666}$ are shown in (F). See also Figures S3–S5.

are able to act independently of one another. Residues that form the hydrophobic pocket are conserved between the N-SH2 and C-SH2 domains (Figure S8), and the corresponding pocket in the C-SH2 domain formed by residues W^{112}, F^{113}, F^{147}, Y^{179}, and L^{190} is occupied by the side chain of the interdomain residue P^{107} (Figures S9A and S9B), bolstered by hydrogen bonding between $T^{108}O^{\gamma1}$ and C-SH2 $T^{191}O^{\gamma1}$ (not shown). These interdomain linker:C-SH2 interactions are also found in crystal structures of pY-peptide-bound SHP2 tandem SH2 domains but not in those of autoinhibited SHP2 (Figure S9D).

2D transverse relaxation optimized spectroscopy (2D-TROSY) solution NMR experiments on the ^{15}N-labeled $SHP2^{1–222}$ tandem domain in the presence and absence of $pY^{627}pY^{659}$-$Gab1^{613–694}$ reveal differences in the spectra in addition to those corresponding to interaction with the peptide. Comparison of the spectra of peptide-bound ^{15}N-labeled $SHP2^{1–222}$ with those of the peptide-bound individual domains allows partial assignment of the tandem domains, revealing resonance shifts compatible with formation of the interface observed in the crystal upon pY-pY Gab1 peptide binding in solution (Figures 6J and S10). Remarkably, a corresponding interface is found in the structure of the closely related tyrosine phosphatase SHP1 (PTPN6, an enzyme expressed primarily in hemopoietic cells) in an open conformation[34] (Figures 6H and 6I), where SHP1 C-SH2 residue P^{142} juxtaposes a similar N-SH2 proline pocket composed of W^4, F^5, F^{39}, Y^{61}, and L^{72} and the interdomain linker residue P^{105} occupies a pocket formed by C-SH2 residues W^{110}, Y^{111}, F^{145}, Y^{176}, and L^{187}, with $T^{106}O^{\gamma1}$ hydrogen forming a hydrogen bond to C-SH2 $T^{188}O^{\gamma1}$ (Figures S9E and S9F). In addition, interdomain linker residue D^{104} makes a salt bridge to R^3 (which corresponds to R^5 in SHP2, Figure S8), suggesting that interactions between conserved residues of the interdomain linker and both SH2 domains could contribute to the formation of the compact conformation seen here.

DISCUSSION

The data presented here sheds light on the interaction between a bis-phosphorylated activator peptide and the N-SH2-C-SH2 tandem domains of SHP2. The $pY^{627}pY^{659}$-$Gab1^{613–694}$ peptide binds the tandem domain $SHP2^{1–222}$ with high affinity, with pY^{627} and pY^{659} binding to N-SH2 and C-SH2, respectively. CSPs for residues of the isotope-labeled peptide around pY^{659} in the presence of the isolated N-SH2 domain (Figure 4A) suggest, however, that both phosphotyrosine residues could bind the N-SH2 domain, providing a possible explanation for the deviation from a 1:1 binding model apparent in the ITC data (see above, Figure 2B).

The N-terminal pY^{627}-Gab1 peptide interacts with N-SH2 in a canonical fashion (Figure 3A), yet perhaps counterintuitively, NMR data indicate that the domain exhibits enhanced dynamics upon phosphopeptide binding (Figure S4). A similar behavior has been observed for PD-1 binding to the SHP2 N-SH2 domain,[21,35] for which it has been postulated that pY binding perturbs a hydrogen bond network in the N-SH2 domain. Opening of the central β-sheet of N-SH2, which would explain the increased dynamic

Please cite this article in press as: Machner et al., Mechanism of SHP2 activation by bis-Tyr-phosphorylated Gab1, Structure (2025), https://doi.org/10.1016/j.str.2025.11.018

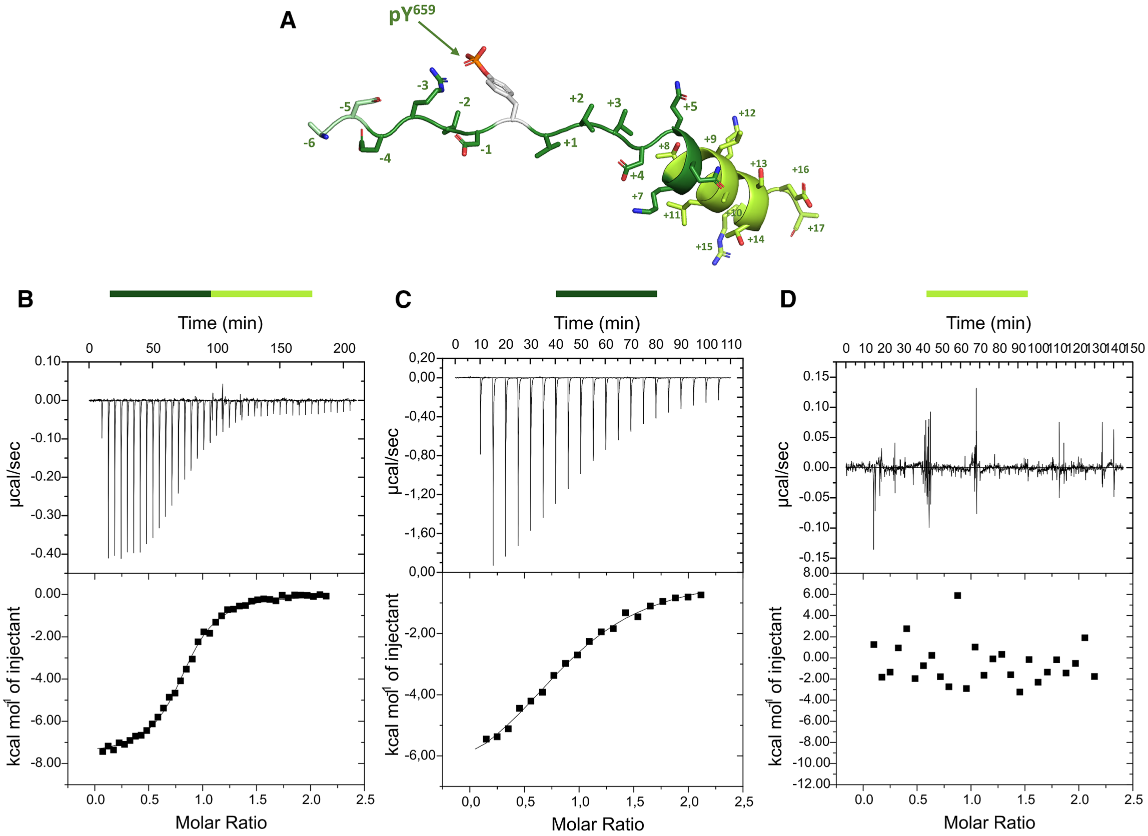

	$\text{C-SH2}^{102\text{-}220}\text{:Gab1}^{655\text{-}677}$	$\text{C-SH2}^{102\text{-}220}\text{:Gab1}^{655\text{-}666}$	$\text{C-SH2}^{102\text{-}220}\text{:Gab1}^{667\text{-}677}$
N	0.89 ± 0.05	1.03 ± 0.08	-
K_D [nM]	4393 ± 337	49252 ± 3325	-
- ΔS · T	515 ± 301	860 ± 129	-
ΔH	-7826 ± 313	-6739 ± 131	-
ΔG	-7310 ± 46	-5878 ± 40	-

Figure 5. Binding of pY^{659}-Gab1 to the SHP2 C-$SH2^{102–220}$ domain analyzed using ITC

(A) Structure of the pY^{659}-$Gab1^{655–676}$ peptide as bound to the C-SH2 domain in crystals of the N-SH2-C-SH2-tandem $SHP2^{1–222}$ construct in complex with $pY^{627}pY^{659}$-$Gab1^{617–684}$ (residues E^{655}-K^{666}, dark green; T^{667}-A^{676}, light green).

(B–D) The monophosphorylated pY^{659}-$Gab1^{655–677}$ binds the C-SH2 domain with micromolar affinity; C-terminal truncation of the peptide to pY^{659}-$Gab1^{655–666}$ results in a 10-fold drop in affinity, whereas the C-terminal peptide $Gab1^{667–677}$ shows no enthalpy change.

behavior of the N-SH2 domain, is thought to relay the peptide-binding signal and has been proposed to play a key role in activation.[36],[37] Propagation of such conformational fluctuations to the DE-loop, which occupies the PTP active site cleft in the autoinhibited state (see Figure S11), could contribute to disengagement of the N-SH2 domain and activation of the phosphatase.[38] A further opening of the EF-loop would allow residues in the activating peptide C-terminal to pY to fully occupy the N-SH2 peptide-binding site, preventing reclosure of the N-SH2:PTP interface.

In contrast to the canonical binding of pY^{627}-Gab1 to the N-SH2 domain, the pY^{659}-Gab1 peptide exhibits a bipartite binding to C-SH2. Gab1 residues adjacent to pY^{659} exhibit an extended conformation, whereas those C-terminal to pY^{659} adopt a helical conformation, where residue D^{663} could facilitate helix initiation through N-capping.[39] Such a binding mode involving concomitant peptide folding and binding may contribute to increased selectivity of the peptide for the C-SH2 domain, requiring an inherent helical propensity that is able to present the correct residues to the target domain, as has, for example, also been proposed for peptide recognition by class 2 G protein-coupled receptors.[40]

An unexpected finding of the present studies was the observation of a compact arrangement of the tandem domain in the presence of the bound $pY^{627}pY^{659}$-$Gab1^{613–694}$ peptide, with a novel N-SH2-C-SH2 domain interface (Figures 6A, 6B, and 6J). Although it is possible that this arrangement could be a result of crystal packing effects, the fact that the same inter-domain contacts are found in the open state of the related

Please cite this article in press as: Machner et al., Mechanism of SHP2 activation by bis-Tyr-phosphorylated Gab1, Structure (2025), https://doi.org/10.1016/j.str.2025.11.018

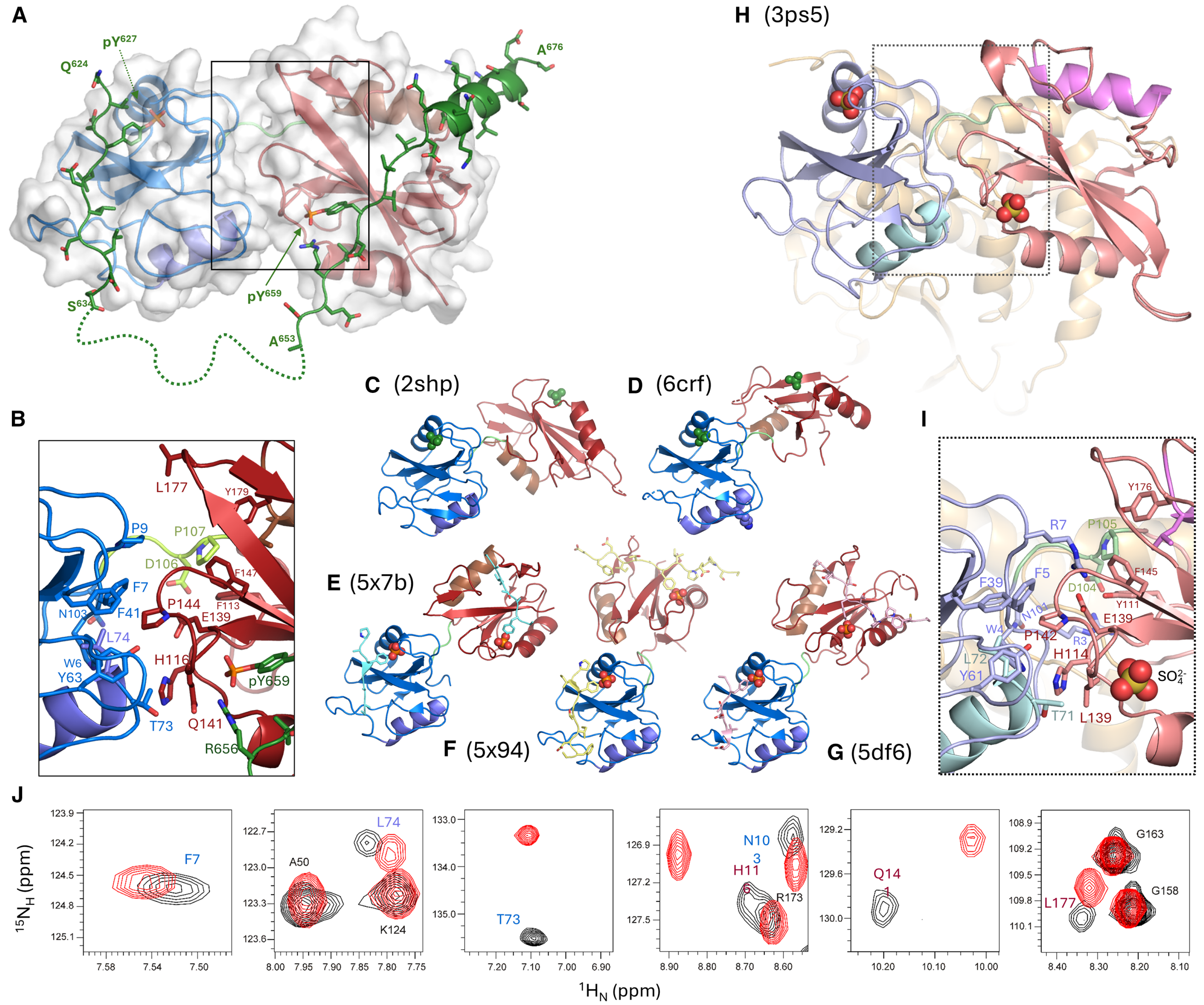

Figure 6. Structures of the SHP2$^{1\text{–}222}$ tandem domain in the presence and absence of activator peptides, aligned through superposition of the N-SH2 domains (blue)

(A and B) (A) The N-SH2-C-SH2 tandem domain SHP2$^{1\text{–}220}$ in the presence of bis-phosphorylated pY^{627}pY^{659}-Gab1$^{617\text{–}683}$ (green; disordered residues Gly^{635}-Val^{652} represented by a dotted line) solved by microcrystal electron diffraction (MicroED, this work). The crystal structure reveals a novel inter-domain interface (B) centered around Pro^{144} that has previously not been observed for SHP2.

(C) SH2 domain arrangement in autoinhibited SHP2,[4] i.e., in the absence of any activator. Nearly all deposited SHP2 structures show this arrangement (not shown).

(D) Relative orientations of the SH2 domains in the constitutively active oncogenic mutant SHP2^{E76K} [5] without activator.

(E–G) SHP2 tandem domains in complex with mono-phosphorylated peptides from *Helicobacter pylori* CagA[17] (E and F) or thioredoxin-interacting protein TXNIP[33] (G).

(H and I) An interface corresponding to that seen here (A and B) is found in an open crystal structure of the related SHP1/PTPN6 enzyme.[34] For orientation, SHP1 helices $\alpha B^{N\text{–}SH2}$ and $\alpha B^{N\text{–}SH2}$ are colored cyan and pink, respectively.

(J) Selected regions of the 2D-TROSY spectra (Figure S10) from ^{15}N-labeled SHP2$^{1\text{–}222}$ (black) in the presence of pY^{627}pY^{659}-Gab1$^{613\text{–}694}$ superimposed on those of the peptide-bound ^{15}N-N-SH2 and ^{15}N-C-SH2 domains (both red). See also Figures S9, S10, and S12.

tyrosine phosphatase SHP1 (PTPN6)[34] (Figures 6H and 6I)—in a completely different protein and crystallographic context—suggests that this is a property of the tandem domains. Indeed, a crystal structure of the SHP2 tandem SH2 domain in complex with the bis-phosphorylated PZR (myelin protein zero-like protein 1)-derived C-terminal peptide,[41] released during the final revision of this manuscript (9mq5), reveals the same arrangement (Figure S12), with an equivalent N-SH2:C-SH2 interface. This is in spite of substantial differences in the activating peptide (the pYpY-PZR peptide has a short 21-residue inter-pY-linker that is almost completely defined in the crystal, and the peptide binding to the C-SH2 domain is "canonical" without a C-terminal helix) and having been solved in a completely different crystal form.

Please cite this article in press as: Machner et al., Mechanism of SHP2 activation by bis-Tyr-phosphorylated Gab1, Structure (2025), https://doi.org/10.1016/j.str.2025.11.018

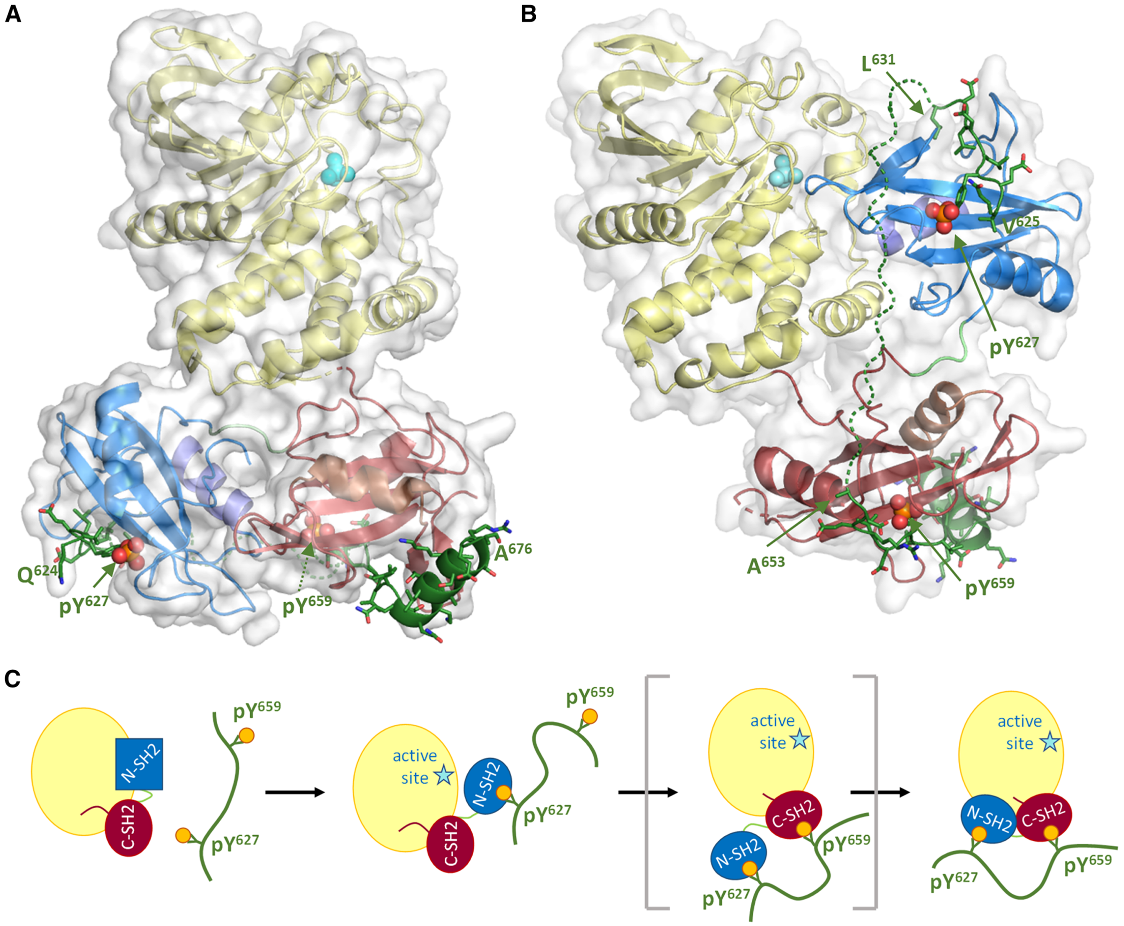

Figure 7. Proposed two-state model for SHP2 activation

(A) Model of the postulated pYpY-Gab1 activated state of SHP2.

(B) Superposition of the two phosphotyrosine peptides to the respective N- and C-SH2 domains in the autoinhibited structure[4] requires an almost fully extended conformation of the intervening 27 residues to allow simultaneous binding to both SH2 domains in this conformation.

(C) Postulated mechanism for the activation of SHP2 by bis-phosphorylated Gab1 (see also Video S1); note that the sequence of events is undefined and serves only as a guide. Binding of pY^{627} destabilizes the N-SH2 domain, resulting in its dissociation from the PTP domain and activation of the phosphotyrosine phosphatase. The C-SH2 domain relocates to its favored position on the catalytic domain, engaging pY^{659}, with the N-SH2 following. The multiple small energetic contributions to each state would allow for rapid conversion between inactive and active states that could be additionally modulated through, e.g., dephosphorylation of the Gab1 peptide. See also Figure S11.

Notably, formation of the interdomain interface is incompatible with the closed conformation of SHP2 (Figures S11A and S11B), where the C-SH2 domain would clash with the PTP domain. Like SHP2, full-length SHP1 adopts an autoinhibited closed state (Figure S11C)[42] with the DE-loop of the N-SH2 domain occupying the PTP active site; the C-SH2 is in a similar location to that in SHP2 but differently oriented. The open form of full-length SHP1 crystallized in the absence of any activators,[34] but sulfate ions from the crystallization buffer occupy the active site and the SH2 phosphotyrosine-binding sites (Figure S11D).

In structures of the oncogenic mutant SHP2 E76K[5] and the N-SH2-lacking construct SHP2 ΔN-SH2,[6] the C-SH2 domains adopt a position relative to the phosphatase domain equivalent to that in the open-state SHP1 structure (Figures S11E and S11F). This observation, supported by mutational data,[43,44] suggests, in turn, that this position of the C-SH2 domain is favored upon disruption of the N-SH2:PTPase domain interaction. Superposition of the pYpY-Gab1-bound SHP2 tandem domain solved here upon that of the SHP2 ΔN-SH2 structure via their C-SH2 domains (Figure S11G) results in a putative full-length SHP2 domain architecture similar to that of the open form of SHP1 (Figure S11D). Considering that the structures discussed here are of substantially different constructs from multiple crystal forms, we postulate that both SHP1 and SHP2 adopt a common active state (Figure 7A, S11D, and S11G). Indeed, residues that make up the interface between the catalytic domain and the two SH2 domains in this conformation are conserved between the two PTPs (Figure S8).[34]

It is of note that in our model, the positioning of the N-SH2 domain is different from that seen in the open form of SHP2^{E76K} [4] (Figures S11E and S11G). It has been suggested that the latter structure might not be representative of active SHP2 in solution,[38] and inspection of the deposited coordinates

Please cite this article in press as: Machner et al., Mechanism of SHP2 activation by bis-Tyr-phosphorylated Gab1, Structure (2025), https://doi.org/10.1016/j.str.2025.11.018

(6crf) suggests that the conformation seen in the crystal may be influenced by the use of an unphysiological C-terminally truncated SHP2 construct for crystallization and not be favorable for full-length SHP2 (Figure S13A). In the presence of the allosteric inhibitor SHP099, SHP2^{E76K} adopts the autoinhibited conformation (6crg),[5] but residues H^{85}-D^{94} of the N-SH2 domain BG-loop, which are structured in wild-type SHP2 (Figure S13B),[4] are disordered (Figures S13C and S13D). As this segment is ordered in structures of wild-type SHP2 in the presence of SHP099 (Figure S13E),[6] we conclude that the mutation E76K destabilizes the autoinhibited state, providing a possible explanation for the constitutive activation of this oncogenic variant.

Availability of a structural model for the open state of SHP2 allows insights into the activation mechanism of the enzyme. Superposition of the two Gab1 phosphotyrosine peptides to the respective N- and C-SH2 domains in the autoinhibited structure (Figure 7B) indicates that the 27-residue disordered (in the tandem domain structure) pYpY-Gab1 linker would have to be almost fully extended in order to engage both SH2 domains in the autoinhibited state simultaneously. We envisage activation in stages (Figure 7C and Video S1): initial binding of the N-terminal pY^{627} peptide destabilizes the N-SH2 domain, leading to its dissociation from the PTP domain. This is in keeping with deep mutational scanning studies that correlate N-SH2 domain destabilization with increased SHP2 basal activity.[44] N-SH2:PTP dissociation would in turn allow the C-SH2 domain to relocate to its "ground-state" position observed in the SHP2 ΔN-SH2 structure[7] as well as facilitate engagement of the Gab1 C-terminal pY^{659} epitope. Positioning of the N-SH2 domain to allow concomitant formation of the C-SH2 domain interface observed here and the PTP domain interface found in the SHP1 open conformation[34] would then result in an activated state that is stabilized by multiple interactions. Clearly, the sequencing of these steps—some of which may occur simultaneously—is at present undetermined.

Although activated SHP2 likely adopts an ensemble of states,[7,45–47] in a first approximation, we can think of SHP2 (and SHP1) as being able to exist predominantly in two states: one closed (with a stabilized N-SH2 domain but unfavorable positioning of the C-SH2 domain) and one open (with a destabilized N-SH2 domain but stabilized N-SH2:C-SH2:PTP-domain contacts). A fine energetic balance between these states would facilitate switching between active and inactive states through ligand binding, which could be fine-tuned to achieve a wide range of signaling outcomes. In contrast to the latent activity of SHP2, SHP1 is active under basal cellular conditions, requiring downregulation upon activation of the signaling cascade.[48] This suggests that the equilibrium between active and inactive states is shifted more toward the former in SHP1, providing an explanation for the manifestation of the open structure in crystals of SHP1.[34]

A number of open issues remain: is the observed compact state of the tandem SH2 domain stable or transient? Additional interactions provided by the presence of the PTP domain—as described for the open form of SHP1—would act synergistically to stabilize the postulated open state, yet is a weakening of the N-SH2:PTP domain interaction in the autoinhibited state sufficient to adopt this conformation? Is a covalent linkage between the N-SH2- and C-SH2-binding pY-peptides necessary? Could the long inter-pY Gab1 peptide linker result in intermolecular networks of SHP2 and potentially SHP2 activation in *trans*? Clearly, application of complementary biophysical techniques such as fluorescence resonance energy transfer experiments, small angle X-ray scattering, paramagnetic NMR investigations, and molecular dynamics studies as well as in-depth enzymatic measurements will be necessary to map the (thermodynamic and kinetic) energetic landscape of this complex system.

SHP2 activation within the cell is presumably a highly dynamic process, regulated by both Gab1 (mono- and bis-) phosphorylation and dephosphorylation. As has been noted for other SHP2 activators, the transition to an active state could be induced through occupation of only one SH2 site. As such, monophosphorylated Gab1 species could elicit alternative activated species. In contrast to the 31 residue inter-pY spacing in Gab1 that would require an extended peptide to occupy both SH2-binding sites in the autoinhibited state, the insulin receptor substrate 1 (IRS-1) harbors a 49-residue inter-pY linker[49] that could easily allow simultaneous binding. On the other hand, the shorter inter-pY linkers found in PD-1 (24 amino acids)[21,22] and PZR (21 amino acids)[41] would preclude concurrent binding of the two phosphotyrosines in the closed state (with the caveat that the C-SH2 domain could adopt alternative positions in solution). It is, therefore, conceivable that differences in linker length (as well as in amino acid composition) could result in nuanced outcomes to orchestrate cell signaling.

Much research has gone into the search for inhibitors of SHP2 due to its association with cancer, and compounds such as SHP099[6] and TNO155[50] that act allosterically by binding all three domains in the closed conformation have attracted considerable attention. The structure of the closed state has also been used to identify an alternative allosteric site at the N-SH2:PTP interface to yield SHP244,[51] which enhances inhibition in cells when used in combination with SHP099. As SHP2 also acts as a tumor suppressor, small molecule activators may exhibit therapeutic potential.[52] Recognition of a defined active state structure paves the way toward not only a better understanding of the activation mechanisms of SHP1 and SHP2 but also the discovery of allosteric activators of these crucial enzymes that can be employed in chemical biological approaches to probe cellular functions and perhaps yield useful anticancer drugs in the future.

RESOURCE AVAILABILITY

Lead contact

Further information and requests for resources and reagents should be directed to and will be fulfilled by the lead contact, Milton T. Stubbs (stubbs@biochemtech.uni-halle.de).

Materials availability

Plasmids generated in this study are available from the lead contact upon reasonable request.

Data and code availability

- Coordinates and structure factors have been deposited to the PDB (codes 9qa5 and 9qcd) and are publicly available as of the date of publication. NMR chemical shift data are publicly available as of the date of publication at the BMRB (IDs 53252–53258).
- This paper does not report original code.
- Any additional information required to reanalyze the data reported in this paper is available from the lead contact upon request.

Please cite this article in press as: Machner et al., Mechanism of SHP2 activation by bis-Tyr-phosphorylated Gab1, Structure (2025), https://doi.org/10.1016/j.str.2025.11.018

ACKNOWLEDGMENTS

This paper is dedicated to the memory of our friend, colleague, and mentor Professor Dr. Wolfram Bode, whose pioneering studies on trypsinogen revealed the importance of order-disorder transitions in protein functions. This research was supported by the DFG RTG 2467 "Intrinsically Disordered Proteins – Molecular Principles, Cellular Functions, and Diseases" (project number 391498659) as well as the SFB TRR 102 and SFB 1664 (DFG—514901783); DFG grants FE439/7-1 and BA 1821/6-1; the BMBF ZIK project HALOmem (grant nos. 03Z22HN23, 03COV04, and 03Z22HI2); the European Regional Development Funds (EFRE) for Saxony-Anhalt (grant no. ZS/2016/04/78115), which also provides funding for the NMR facility of the Martin-Luther-University (grant no. 2.21.6.05.00056); the Halle - Oxford (HAL-OX) Research Network "Disease Biology and Molecular Medicine" funded by the EU/ESF; and the Horizon Europe ERA Chair "hot4cryo" (project number 101086665). The authors gratefully acknowledge Dr. Ioannis Skalidis for suggesting the use of 3D electron diffraction, the success of which was central to this project; PD Dr. Annette Meister for advice on vitrification; as well as all three reviewers for their insightful and constructive comments.

AUTHOR CONTRIBUTIONS

J.B., S.M.F., P.L.K., L.M., and M.T.S. designed the experiments. L.M., J.K., F.W., and M.L. expressed and purified the proteins and conducted the ITC measurements. L.M. performed the NMR experiments under the supervision of T.G. L.M. and J.K. crystallized the peptide-protein complexes. F.L.K., F.H., and A.S. optimized the sample vitrification, which was performed by F.L.K. F.H. carried out electron microscopic alignment and adjustments and implemented the diffraction protocols. F.H. and A.S. performed the ED data collection. A.S., C.P., and L.M. processed and analyzed the electron diffraction data. A.S., C.B., and L.M. solved the structures and refined the models. L.M. and M.T.S. drafted the manuscript. J.B., S.M.F., P.L.K., and M.T.S. supervised the project and revised the manuscript.

DECLARATION OF INTERESTS

The authors declare no competing interests.

STAR★METHODS

Detailed methods are provided in the online version of this paper and include the following:

- KEY RESOURCES TABLE
- EXPERIMENTAL MODEL AND STUDY PARTICIPANT DETAILS
- METHOD DETAILS
    - ○ Protein expression and purification
    - ○ Expression and purification of Murine Abl kinase for peptide phosphorylation
    - ○ Expression and purification of SHP2 SH2 domains
    - ○ Isothermal titration calorimetry
    - ○ X-ray crystallography of N-SH2: pY^{627}-Gab1 complex
    - ○ 3D electron diffraction of SHP2 tandem SH2: pYpY-Gab1
    - ○ NMR spectroscopy
    - ○ Modelling of Gab1-bound SHP2
- QUANTIFICATION AND STATISTICAL ANALYSIS

SUPPLEMENTAL INFORMATION

Supplemental information can be found online at https://doi.org/10.1016/j.str.2025.11.018.

Received: April 23, 2025
Revised: September 30, 2025
Accepted: November 26, 2025

REFERENCES

1. Asmamaw, M.D., Shi, X.-J., Zhang, L.-R., and Liu, H.-M. (2022). A comprehensive review of SHP2 and its role in cancer. Cell. Oncol. *45*, 729–753. https://doi.org/10.1007/s13402-022-00698-1.
2. Saint-Laurent, C., Mazeyrie, L., Tajan, M., Paccoud, R., Castan-Laurell, I., Valet, P., Edouard, T., Pradère, J.-P., Dray, C., and Yart, A. (2022). The Tyrosine Phosphatase SHP2: A New Target for Insulin Resistance? Biomedicines *10*, 2139. https://doi.org/10.3390/biomedicines10092139.
3. Poole, A.W., and Jones, M.L. (2005). A SHPing tale: perspectives on the regulation of SHP-1 and SHP-2 tyrosine phosphatases by the C-terminal tail. Cell. Signal. *17*, 1323–1332. https://doi.org/10.1016/j.cellsig.2005.05.016.
4. Hof, P., Pluskey, S., Dhe-Paganon, S., Eck, M.J., and Shoelson, S.E. (1998). Crystal structure of the tyrosine phosphatase SHP-2. Cell *92*, 441–450. https://doi.org/10.1016/s0092-8674(00)80938-1.
5. LaRochelle, J.R., Fodor, M., Vemulapalli, V., Mohseni, M., Wang, P., Stams, T., LaMarche, M.J., Chopra, R., Acker, M.G., and Blacklow, S.C. (2018). Structural reorganization of SHP2 by oncogenic mutations and implications for oncoprotein resistance to allosteric inhibition. Nat. Commun. *9*, 4508. https://doi.org/10.1038/s41467-018-06823-9.
6. Chen, Y.-N.P., LaMarche, M.J., Chan, H.M., Fekkes, P., Garcia-Fortanet, J., Acker, M.G., Antonakos, B., Chen, C.H.-T., Chen, Z., Cooke, V.G., et al. (2016). Allosteric inhibition of SHP2 phosphatase inhibits cancers driven by receptor tyrosine kinases. Nature *535*, 148–152. https://doi.org/10.1038/nature18621.
7. Pádua, R.A.P., Sun, Y., Marko, I., Pitsawong, W., Stiller, J.B., Otten, R., and Kern, D. (2018). Mechanism of activating mutations and allosteric drug inhibition of the phosphatase SHP2. Nat. Commun. *9*, 4507. https://doi.org/10.1038/s41467-018-06814-w.
8. Tartaglia, M., Mehler, E.L., Goldberg, R., Zampino, G., Brunner, H.G., Kremer, H., van der Burgt, I., Crosby, A.H., Ion, A., Jeffery, S., et al. (2001). Mutations in PTPN11, encoding the protein tyrosine phosphatase SHP-2, cause Noonan syndrome. Nat. Genet. *29*, 465–468. https://doi.org/10.1038/ng772.
9. Tartaglia, M., Martinelli, S., Stella, L., Bocchinfuso, G., Flex, E., Cordeddu, V., Zampino, G., Burgt, I.v.d., Palleschi, A., Petrucci, T.C., et al. (2006). Diversity and functional consequences of germline and somatic PTPN11 mutations in human disease. Am. J. Hum. Genet. *78*, 279–290. https://doi.org/10.1086/499925.
10. Keilhack, H., David, F.S., McGregor, M., Cantley, L.C., and Neel, B.G. (2005). Diverse biochemical properties of Shp2 mutants. Implications for disease phenotypes. J. Biol. Chem. *280*, 30984–30993. https://doi.org/10.1074/jbc.M504699200.
11. Higashi, H., Tsutsumi, R., Muto, S., Sugiyama, T., Azuma, T., Asaka, M., and Hatakeyama, M. (2002). SHP-2 tyrosine phosphatase as an intracellular target of Helicobacter pylori CagA protein. Science (New York, N.Y.) *295*, 683–686. https://doi.org/10.1126/science.1067147.
12. Nagase, L., Hayashi, T., Senda, T., and Hatakeyama, M. (2015). Dramatic increase in SHP2 binding activity of Helicobacter pylori Western CagA by EPIYA-C duplication: its implications in gastric carcinogenesis. Sci. Rep. *5*, 15749. https://doi.org/10.1038/srep15749.
13. Chen, X., Fu, X., Zhao, W., Ho, W.-T.T., Xing, S., and Zhao, Z.J. (2020). Loss of tyrosine phosphatase SHP2 activity promotes growth of colorectal carcinoma HCT-116 cells. Signal Transduct. Target. Ther. *5*, 83. https://doi.org/10.1038/s41392-020-0192-0.
14. Bard-Chapeau, E.A., Li, S., Ding, J., Zhang, S.S., Zhu, H.H., Princen, F., Fang, D.D., Han, T., Bailly-Maitre, B., Poli, V., et al. (2011). Ptpn11/Shp2 acts as a tumor suppressor in hepatocellular carcinogenesis. Cancer Cell *19*, 629–639. https://doi.org/10.1016/j.ccr.2011.03.023.
15. Chen, Y., Wen, R., Yang, S., Schuman, J., Zhang, E.E., Yi, T., Feng, G.-S., and Wang, D. (2003). Identification of Shp-2 as a Stat5A phosphatase. J. Biol. Chem. *278*, 16520–16527. https://doi.org/10.1074/jbc.M210572200.

Please cite this article in press as: Machner et al., Mechanism of SHP2 activation by bis-Tyr-phosphorylated Gab1, Structure (2025), https://doi.org/10.1016/j.str.2025.11.018

16. Barford, D., and Neel, B.G. (1998). Revealing mechanisms for SH2 domain mediated regulation of the protein tyrosine phosphatase SHP-2. Structure *6*, 249–254. https://doi.org/10.1016/s0969-2126(98)00027-6.
17. Hayashi, T., Senda, M., Suzuki, N., Nishikawa, H., Ben, C., Tang, C., Nagase, L., Inoue, K., Senda, T., and Hatakeyama, M. (2017). Differential Mechanisms for SHP2 Binding and Activation Are Exploited by Geographically Distinct Helicobacter pylori CagA Oncoproteins. Cell Rep. *20*, 2876–2890. https://doi.org/10.1016/j.celrep.2017.08.080.
18. Sugimoto, S., Wandless, T.J., Shoelson, S.E., Neel, B.G., and Walsh, C.T. (1994). Activation of the SH2-containing protein tyrosine phosphatase, SH-PTP2, by phosphotyrosine-containing peptides derived from insulin receptor substrate-1. J. Biol. Chem. *269*, 13614–13622. https://doi.org/10.1016/S0021-9258(17)36874-6.
19. Ohnishi, H., Kubota, M., Ohtake, A., Sato, K., and Sano, S.i. (1996). Activation of protein-tyrosine phosphatase SH-PTP2 by a tyrosine-based activation motif of a novel brain molecule. J. Biol. Chem. *271*, 25569–25574. https://doi.org/10.1074/jbc.271.41.25569.
20. Ottinger, E.A., Botfield, M.C., and Shoelson, S.E. (1998). Tandem SH2 domains confer high specificity in tyrosine kinase signaling. J. Biol. Chem. *273*, 729–735. https://doi.org/10.1074/jbc.273.2.729.
21. Marasco, M., Berteotti, A., Weyershaeuser, J., Thorausch, N., Sikorska, J., Krausze, J., Brandt, H.J., Kirkpatrick, J., Rios, P., Schamel, W.W., et al. (2020). Molecular mechanism of SHP2 activation by PD-1 stimulation. Sci. Adv. *6*, eaay4458. https://doi.org/10.1126/sciadv.aay4458.
22. Patsoukis, N., Duke-Cohan, J.S., Chaudhri, A., Aksoylar, H.-I., Wang, Q., Council, A., Berg, A., Freeman, G.J., and Boussiotis, V.A. (2020). Interaction of SHP-2 SH2 domains with PD-1 ITSM induces PD-1 dimerization and SHP-2 activation. Commun. Biol. *3*, 128. https://doi.org/10.1038/s42003-020-0845-0.
23. Holgado-Madruga, M., Emlet, D.R., Moscatello, D.K., Godwin, A.K., and Wong, A.J. (1996). A Grb2-associated docking protein in EGF- and insulin-receptor signalling. Nature *379*, 560–564. https://doi.org/10.1038/379560a0.
24. Liu, Y., and Rohrschneider, L.R. (2002). The gift of Gab. FEBS Lett. *515*, 1–7. https://doi.org/10.1016/s0014-5793(02)02425-0.
25. Cunnick, J.M., Mei, L., Doupnik, C.A., and Wu, J. (2001). Phosphotyrosines 627 and 659 of Gab1 constitute a bisphosphoryl tyrosine-based activation motif (BTAM) conferring binding and activation of SHP2. J. Biol. Chem. *276*, 24380–24387. https://doi.org/10.1074/jbc.M010275200.
26. Simister, P.C., and Feller, S.M. (2012). Order and disorder in large multisite docking proteins of the Gab family–implications for signalling complex formation and inhibitor design strategies. Mol. Biosyst. *8*, 33–46. https://doi.org/10.1039/c1mb05272a.
27. Le Goff, A., Ji, Z., Leclercq, B., Bourette, R.P., Mougel, A., Guerardel, C., de Launoit, Y., Vicogne, J., Goormachtigh, G., and Fafeur, V. (2012). Anti-apoptotic role of caspase-cleaved GAB1 adaptor protein in hepatocyte growth factor/scatter factor-MET receptor protein signaling. J. Biol. Chem. *287*, 35382–35396. https://doi.org/10.1074/jbc.M112.409797.
28. Gruber, T., Lewitzky, M., Machner, L., Weininger, U., Feller, S.M., and Balbach, J. (2022). Macromolecular Crowding Induces a Binding Competent Transient Structure in Intrinsically Disordered Gab1. J. Mol. Biol. *434*, 167407. https://doi.org/10.1016/j.jmb.2021.167407.
29. Waksman, G., Kumaran, S., and Lubman, O. (2004). SH2 domains: role, structure and implications for molecular medicine. Expert Rev. Mol. Med. *6*, 1–18. https://doi.org/10.1017/S1462399404007331.
30. Clabbers, M.T.B., and Xu, H. (2020). Microcrystal electron diffraction in macromolecular and pharmaceutical structure determination. Drug Discov. Today Technol. *37*, 93–105. https://doi.org/10.1016/j.ddtec.2020.12.002.
31. Shaikhqasem, A., Hamdi, F., Machner, L., Parthier, C., Breithaupt, C., Kyrilis, F.L., Feller, S.M., Kastritis, P.L., and Stubbs, M.T. (2026). Strategies for Mitigating Radiation Damage and Improving Data Completeness in 3D Electron Diffraction of Protein Crystals. Acta Cryst. D. https://doi.org/10.1107/S2059798325011258.
32. Shi, D., Nannenga, B.L., Iadanza, M.G., and Gonen, T. (2013). Three-dimensional electron crystallography of protein microcrystals. eLife *2*, e01345. https://doi.org/10.7554/eLife.01345.
33. Liu, Y., Lau, J., Li, W., Tempel, W., Li, L., Dong, A., Narula, A., Qin, S., and Min, J. (2016). Structural basis for the regulatory role of the PPxY motifs in the thioredoxin-interacting protein TXNIP. Biochem. J. *473*, 179–187. https://doi.org/10.1042/BJ20150830.
34. Wang, W., Liu, L., Song, X., Mo, Y., Komma, C., Bellamy, H.D., Zhao, Z.J., and Zhou, G.W. (2011). Crystal structure of human protein tyrosine phosphatase SHP-1 in the open conformation. J. Cell. Biochem. *112*, 2062–2071. https://doi.org/10.1002/jcb.23125.
35. Marasco, M., Kirkpatrick, J., Nanna, V., Sikorska, J., and Carlomagno, T. (2021). Phosphotyrosine couples peptide binding and SHP2 activation via a dynamic allosteric network. Comput. Struct. Biotechnol. J. *19*, 2398–2415. https://doi.org/10.1016/j.csbj.2021.04.040.
36. Anselmi, M., and Hub, J.S. (2021). The loops of the N-SH2 binding cleft do not serve as allosteric switch in SHP2 activation. Proc. Natl. Acad. Sci. USA *118*, e2025107118. https://doi.org/10.1073/pnas.2025107118.
37. Marasco, M., Kirkpatrick, J., Carlomagno, T., Hub, J.S., and Anselmi, M. (2024). Phosphopeptide binding to the N-SH2 domain of tyrosine phosphatase SHP2 correlates with the unzipping of its central β-sheet. Comput. Struct. Biotechnol. J. *23*, 1169–1180. https://doi.org/10.1016/j.csbj.2024.02.023.
38. Calligari, P., Santucci, V., Stella, L., and Bocchinfuso, G. (2021). Discriminating between competing models for the allosteric regulation of oncogenic phosphatase SHP2 by characterizing its active state. Comput. Struct. Biotechnol. J. *19*, 6125–6139. https://doi.org/10.1016/j.csbj.2021.10.041.
39. Presta, L.G., and Rose, G.D. (1988). Helix signals in proteins. Science (New York, N.Y.) *240*, 1632–1641. https://doi.org/10.1126/science.2837824.
40. Parthier, C., Kleinschmidt, M., Neumann, P., Rudolph, R., Manhart, S., Schlenzig, D., Fanghänel, J., Rahfeld, J.-U., Demuth, H.-U., and Stubbs, M.T. (2007). Crystal structure of the incretin-bound extracellular domain of a G protein-coupled receptor. Proc. Natl. Acad. Sci. USA *104*, 13942–13947. https://doi.org/10.1073/pnas.0706404104.
41. Perla, S., Stiegler, A.L., Yi, J.-S., Enyenihi, L., Zhang, L., Riaz, M., An, E., Qyang, Y., Boggon, T.J., and Bennett, A.M. (2025). SHP2 genetic variants in NSML-associated RASopathies disrupt the PZR-IRX transcription factor signaling axis. Proc. Natl. Acad. Sci. USA *122*, e2503631122. https://doi.org/10.1073/pnas.2503631122.
42. Yang, J., Liu, L., He, D., Song, X., Liang, X., Zhao, Z.J., and Zhou, G.W. (2003). Crystal structure of human protein-tyrosine phosphatase SHP-1. J. Biol. Chem. *278*, 6516–6520. https://doi.org/10.1074/jbc.M210430200.
43. Kim, S.H., Bulos, M.L., Adams, J.A., Yun, B.K., and Bishop, A.C. (2024). Single Ion Pair Is Essential for Stabilizing SHP2's Open Conformation. Biochemistry *63*, 273–281. https://doi.org/10.1021/acs.biochem.3c00609.
44. Jiang, Z., van Vlimmeren, A.E., Karandur, D., Semmelman, A., and Shah, N.H. (2025). Deep mutational scanning of the multi-domain phosphatase SHP2 reveals mechanisms of regulation and pathogenicity. Nat. Commun. *16*, 5464. https://doi.org/10.1038/s41467-025-60641-4.
45. Anselmi, M., and Hub, J.S. (2023). Atomistic ensemble of active SHP2 phosphatase. Commun. Biol. *6*, 1289. https://doi.org/10.1038/s42003-023-05682-5.
46. Tao, Y., Xie, J., Zhong, Q., Wang, Y., Zhang, S., Luo, F., Wen, F., Xie, J., Zhao, J., Sun, X., et al. (2021). A novel partially open state of SHP2 points to a "multiple gear" regulation mechanism. J. Biol. Chem. *296*, 100538. https://doi.org/10.1016/j.jbc.2021.100538.
47. LaRochelle, J.R., Fodor, M., Xu, X., Durzynska, I., Fan, L., Stams, T., Chan, H.M., LaMarche, M.J., Chopra, R., Wang, P., et al. (2016). Structural and Functional Consequences of Three Cancer-Associated Mutations of the Oncogenic Phosphatase SHP2. Biochemistry *55*, 2269–2277. https://doi.org/10.1021/acs.biochem.5b01287.

Please cite this article in press as: Machner et al., Mechanism of SHP2 activation by bis-Tyr-phosphorylated Gab1, Structure (2025), https://doi.org/10.1016/j.str.2025.11.018

48. Jones, M.L., Craik, J.D., Gibbins, J.M., and Poole, A.W. (2004). Regulation of SHP-1 tyrosine phosphatase in human platelets by serine phosphorylation at its C terminus. J. Biol. Chem. *279*, 40475–40483. https://doi.org/10.1074/jbc.M402970200.
49. Pluskey, S., Wandless, T.J., Walsh, C.T., and Shoelson, S.E. (1995). Potent stimulation of SH-PTP2 phosphatase activity by simultaneous occupancy of both SH2 domains. J. Biol. Chem. *270*, 2897–2900. https://doi.org/10.1074/jbc.270.7.2897.
50. LaMarche, M.J., Acker, M., Argintaru, A., Bauer, D., Boisclair, J., Chan, H., Chen, C.H.-T., Chen, Y.-N., Chen, Z., Deng, Z., et al. (2020). Identification of TNO155, an Allosteric SHP2 Inhibitor for the Treatment of Cancer. J. Med. Chem. *63*, 13578–13594. https://doi.org/10.1021/acs.jmedchem.0c01170.
51. Fodor, M., Price, E., Wang, P., Lu, H., Argintaru, A., Chen, Z., Glick, M., Hao, H.-X., Kato, M., Koenig, R., et al. (2018). Dual Allosteric Inhibition of SHP2 Phosphatase. ACS Chem. Biol. *13*, 647–656. https://doi.org/10.1021/acschembio.7b00980.
52. Guo, W., and Xu, Q. (2020). Phosphatase-independent functions of SHP2 and its regulation by small molecule compounds. J. Pharmacol. Sci. *144*, 139–146. https://doi.org/10.1016/j.jphs.2020.06.002.
53. Yu, Z.-H., Xu, J., Walls, C.D., Chen, L., Zhang, S., Zhang, R., Wu, L., Wang, L., Liu, S., and Zhang, Z.-Y. (2013). Structural and mechanistic insights into LEOPARD syndrome-associated SHP2 mutations. J. Biol. Chem. *288*, 10472–10482. https://doi.org/10.1074/jbc.M113.450023.
54. Tan, X., Zheng, N., Hayashi, K., Cook, W.J., Jeffrey, L.C., Kasperek, E., Pickart, C.M., Mietzsch, M., Agbandje-McKenna, M., Chen, Q., et al. (2008). Worldwide Protein Data Bank. https://doi.org/10.2210/pdb4GWF/pdb.
55. Welch, P.J., and Wang, J.Y. (1993). A C-terminal protein-binding domain in the retinoblastoma protein regulates nuclear c-Abl tyrosine kinase in the cell cycle. Cell *75*, 779–790. https://doi.org/10.1016/0092-8674(93)90497-e.
56. Gopalasingam, P. (2015). Structural Characterization of the Protein Tyrosine Phosphatase Shp2 in Solution (University of Birmingham).
57. Delaglio, F., Grzesiek, S., Vuister, G.W., Zhu, G., Pfeifer, J., and Bax, A. (1995). NMRPipe: a multidimensional spectral processing system based on UNIX pipes. J. Biomol. NMR *6*, 277–293. https://doi.org/10.1007/bf00197809.
58. Maciejewski, M.W., Schuyler, A.D., Gryk, M.R., Moraru, I.I., Romero, P.R., Ulrich, E.L., Eghbalnia, H.R., Livny, M., Delaglio, F., and Hoch, J.C. (2017). NMRbox: A Resource for Biomolecular NMR Computation. Biophys. J. *112*, 1529–1534. https://doi.org/10.1016/j.bpj.2017.03.011.
59. d'Auvergne, E.J., and Gooley, P.R. (2008). Optimisation of NMR dynamic models II. A new methodology for the dual optimisation of the model-free parameters and the Brownian rotational diffusion tensor. J. Biomol. NMR *40*, 121–133. https://doi.org/10.1007/s10858-007-9213-3.
60. Emsley, P., Lohkamp, B., Scott, W.G., and Cowtan, K. (2010). Features and development of Coot. Acta Crystallogr. D Biol. Crystallogr. *66*, 486–501. https://doi.org/10.1107/S0907444910007493.
61. Kabsch, W. (2010). XDS. Acta Crystallogr. D Biol. Crystallogr. *66*, 125–132. https://doi.org/10.1107/S0907444909047337.
62. McCoy, A.J., Grosse-Kunstleve, R.W., Adams, P.D., Winn, M.D., Storoni, L.C., and Read, R.J. (2007). Phaser crystallographic software. J. Appl. Crystallogr. *40*, 658–674. https://doi.org/10.1107/S0021889807021206.
63. Liebschner, D., Afonine, P.V., Baker, M.L., Bunkóczi, G., Chen, V.B., Croll, T.I., Hintze, B., Hung, L.W., Jain, S., McCoy, A.J., et al. (2019). Macromolecular structure determination using X-rays, neutrons and electrons: recent developments in Phenix. Acta Crystallogr. D Struct. Biol. *75*, 861–877. https://doi.org/10.1107/S2059798319011471.
64. Potterton, L., Agirre, J., Ballard, C., Cowtan, K., Dodson, E., Evans, P.R., Jenkins, H.T., Keegan, R., Krissinel, E., Stevenson, K., et al. (2018). CCP4i2: the new graphical user interface to the CCP4 program suite. Acta Crystallogr. D Struct. Biol. *74*, 68–84. https://doi.org/10.1107/S2059798317016035.
65. Murshudov, G.N., Skubák, P., Lebedev, A.A., Pannu, N.S., Steiner, R.A., Nicholls, R.A., Winn, M.D., Long, F., and Vagin, A.A. (2011). REFMAC5 for the refinement of macromolecular crystal structures. Acta Crystallogr. D Biol. Crystallogr. *67*, 355–367. https://doi.org/10.1107/S0907444911001314.
66. Mirdita, M., Schütze, K., Moriwaki, Y., Heo, L., Ovchinnikov, S., and Steinegger, M. (2022). ColabFold: making protein folding accessible to all. Nat. Methods *19*, 679–682. https://doi.org/10.1038/s41592-022-01488-1.
67. Okegawa, Y., and Motohashi, K. (2015). A simple and ultra-low cost homemade seamless ligation cloning extract (SLiCE) as an alternative to a commercially available seamless DNA cloning kit. Biochem. Biophys. Rep. *4*, 148–151. https://doi.org/10.1016/j.bbrep.2015.09.005.
68. Seeliger, M.A., Young, M., Henderson, M.N., Pellicena, P., King, D.S., Falick, A.M., and Kuriyan, J. (2005). High yield bacterial expression of active c-Abl and c-Src tyrosine kinases. Protein Sci. *14*, 3135–3139. https://doi.org/10.1110/ps.051750905.
69. Kröner, F., and Hubbuch, J. (2013). Systematic generation of buffer systems for pH gradient ion exchange chromatography and their application. J. Chromatogr. A *1285*, 78–87. https://doi.org/10.1016/j.chroma.2013.02.017.
70. Albanese, S.K., Parton, D.L., Işık, M., Rodríguez-Laureano, L., Hanson, S.M., Behr, J.M., Gradia, S., Jeans, C., Levinson, N.M., Seeliger, M.A., and Chodera, J.D. (2018). An Open Library of Human Kinase Domain Constructs for Automated Bacterial Expression. Biochemistry *57*, 4675–4689. https://doi.org/10.1021/acs.biochem.7b01081.
71. Clabbers, M.T.B., Shiriaeva, A., and Gonen, T. (2022). MicroED: conception, practice and future opportunities. IUCrJ *9*, 169–179. https://doi.org/10.1107/S2052252521013063.
72. Johnson, B.A. (2004). Using NMRView to visualize and analyze the NMR spectra of macromolecules. Methods Mol. Biol. *278*, 313–352. https://doi.org/10.1385/1-59259-809-9:313.
73. Luca, S., Filippov, D.V., van Boom, J.H., Oschkinat, H., de Groot, H.J., and Baldus, M. (2001). Secondary chemical shifts in immobilized peptides and proteins: a qualitative basis for structure refinement under magic angle spinning. J. Biomol. NMR *20*, 325–331. https://doi.org/10.1023/A:1011278317489.
74. Hendus-Altenburger, R., Fernandes, C.B., Bugge, K., Kunze, M.B.A., Boomsma, W., and Kragelund, B.B. (2019). Random coil chemical shifts for serine, threonine and tyrosine phosphorylation over a broad pH range. J. Biomol. NMR *73*, 713–725. https://doi.org/10.1007/s10858-019-00283-z.
75. Niklasson, M., Otten, R., Ahlner, A., Andresen, C., Schlagnitweit, J., Petzold, K., and Lundström, P. (2017). Comprehensive analysis of NMR data using advanced line shape fitting. J. Biomol. NMR *69*, 93–99. https://doi.org/10.1007/s10858-017-0141-6.
76. Lipari, G., and Szabo, A. (1982). Model-free approach to the interpretation of nuclear magnetic resonance relaxation in macromolecules. 2. Analysis of experimental results. J. Am. Chem. Soc. *104*, 4559–4570. https://doi.org/10.1021/ja00381a010.

Please cite this article in press as: Machner et al., Mechanism of SHP2 activation by bis-Tyr-phosphorylated Gab1, Structure (2025), https://doi.org/10.1016/j.str.2025.11.018

STAR★METHODS

KEY RESOURCES TABLE

REAGENT or RESOURCE	SOURCE	IDENTIFIER
Bacterial and virus strains		
Escherichia coli BL21(DE3) competent cells	Thermo Scientific	Cat#EC0114
Escherichia coli XL10 Gold	Agilent	Cat#200315
Chemicals, peptides, and recombinant proteins		
Acrylamide/Bis solution 30 (29:1)	Roth	A124
Acrylamide/Bis solution 30 (37.5:1)	Roth	Cat#3029
Adenosin-5′-triphosphate disodium salt (ATP)	Roth	HN35.3; CAS 987-65-5
Difco-Agar	Becton Dickinson	Cat#214010
Ammonium acetate	Roth	Cat#7869; CAS 631-61-8
Ammonium chloride	Roth	K298; CAS 12125-02-9
Ammonium-^{15}N chloride	Sigma-Aldrich	Cat#299251; CAS 39466-62-1
Ammonium sulfate	Sigma-Aldrich	A4915; CAS 7783-20-2
Antipain dihydrochloride	Roth	Cat#2933; CAS 37682-72-7
Ammonium peroxydisulphate (APS)	Roth	Cat#9592; CAS 7727-54-0
BIS-TRIS	Roth	Cat#9140; CAS 6976-37-0
Chelating Sepharose FF	Cytiva Life Sciences	Cat#17057501
Cobalt (II) sulphate heptahydrate	Sigma	C6768; CAS 10026-24-1
Deuterium Oxide	Cortecnet	CD5251; CAS 7789-20-0
1,4-Dimethylpiperazine	Sigma-Aldrich	D179302; CAS: 106-58-1
Ethylenediamine	Sigma-Aldrich	Cat#8.00947; CAS 107-15-3
D(+)-Glucose monohydrate	Roth	Cat#6887; CAS 77938-63-7
D-Glucose-13C6	Cortecnet	CC860; CAS 110187-42-3
Hydroxylamine solution	Sigma-Aldrich	Cat#438227; CAS 7803-49-8
Imidazole	Roth	Cat#3899; CAS 288-32-4
Iron (III) chloride hexahydrate	Sigma-Aldrich	F1513; CAS 10025-77-1
Isopropyl β-D-1-thiogalactopyranoside (IPTG)	Roth	Cat#2316; CAS 367-93-1
Kanamycin sulphate	Roth	T832; CAS 25389-94-0
Leupeptin hemisulphate	Roth	CN33; CAS 103476-89-7
Magnesium chloride hexahydrate	Roth	Cat#2189; CAS 7791-18-6
Magnesium sulfate heptahydrate	Sigma-Aldrich	Cat#230391; CAS 10034-99-8
Manganese (II) chloride tetrahydrate	Sigma-Aldrich	M3634; CAS 13446-34-9
2-Mercaptoethanol	Roth	Cat#4227; CAS 60-24-2
Methanol	Roth	HN41; CAS 67-56-1
Methylamine	Sigma-Aldrich	Cat#8.22091
1-Methylpiperazine	Sigma-Aldrich	Cat#130001; CAS: 109-01-3
Nickel (II) sulfate hexahydrate	Sigma-Aldrich	N4882; CAS 10101-97-0
Pepstatin	Roche	Cat#11524488001; CAS 26305-03-3
Phos-tag Acrylamide	WAKO Chemicals	AAL-107
Phenylmethyl sulphonyl fluoride (PMSF)	Roth	Cat#6367; CAS 329-98-6
Poly(ethylene glycol) 3350	Sigma-Aldrich	P4338; CAS 25322-68-3
Potassium dihydrogen phosphate	Roth	Cat#3904; CAS 7778-77-0
2-Propanol	Roth	1HPK; CAS 67-63-0
Sodium acetate	Roth	Cat#6773; CAS 127-09-3
Sodium carbonate	Sigma-Aldrich	Cat#223484; CAS 497-19-8
Sodium chloride	Roth	Cat#9265; CAS 7647-14-5
Sodium citrate tribasic dihydrate	Sigma-Aldrich	C8532; CAS 6132-04-3

(*Continued on next page*)

Please cite this article in press as: Machner et al., Mechanism of SHP2 activation by bis-Tyr-phosphorylated Gab1, Structure (2025), https://doi.org/10.1016/j.str.2025.11.018

Continued

REAGENT or RESOURCE	SOURCE	IDENTIFIER
Sodium hydrogen carbonate	Roth	Cat#6885; CAS 144-55-8
Sodium hydroxide	Roth	Cat#6771; CAS 1310-73-2
Sodium molybdate dihydrate	Roth	Cat#0845; CAS 10102-40-6
Sodium orthovanadate	Sigma-Aldrich	S6508; CAS 13721-39-6
Sodium phosphate, dibasic	Roth	Cat#4984; CAS 10028-24-7
Sodium 3-(trimethylsilyl)-1-propanesulfonate (DSS)	Cortecnet	DSSPF; CAS 2039-96-5
Sodium dodecyl sulphate	Roth	Cat#0183; CAS 151-21-3
N,N,N′,N′-Tetramethylethylenediamine (TEMED)	Roth	Cat#2367; CAS 110-18-9
Thiamine hydrochloride	Sigma-Aldrich	T1270; CAS 67-03-8
Tris-(2-carboxyethyl)-phosphine hydrochloride (TCEP)	Roth	HN95.2; CAS 51805-45-9
Tris-(hydroxymethyl)-amino methane (TRIS)	Roth	Cat#5429; CAS 77-86-1
N-Tris(hydroxymethyl)-methyl-glycine (TRICINE)	Roth	Cat#6977; CAS 5704-04-1
Urea	Roth	Cat#2317; CAS 57-13-6
LB Broth (Luria/Miller), granulated	Roth	Cat# 6673
Terrific Broth modified (TB)	Roth	HP61
Gab1 655-677, pY659 (ProteoGenix, France)	This study	N/A
Gab1 655-666, pY659 (ProteoGenix, France)	This study	N/A
Gab1 667-677 (ProteoGenix, France)	This study	N/A
Gab1 613-651, pY627 (Davids Biotechnologie, Germany)	This study	N/A
Gab1 640-694, pY659 (Davids Biotechnologie, Germany)	This study	N/A
3C Protease	Thermo Fisher	Cat#88947
Aprotinin	Roth	A162; CAS 9087-70-1
Benzonase® Nuclease	Sigma-Aldrich	E1014; CAS 9025-65-4
Lysozyme	Roth	Cat#8259; CAS 12650-88-3
SUMO Protease	Abbkine Scientific	Cat#PRP3001-5000
TEV Protease	New England Biolabs	Cat#P8112S
Critical commercial assays		
QIAprep Spin Miniprep Kit	Qiagen	27104
QuickChange Site-Directed Mutagenesis Kit	Agilent	200518
JBScreen Classic 1-10	Jena Bioscience	CS-114 L
Crystal Screen 1+2	Hampton Research	HR2-130
Index Screen	Hampton Research	HR2-144
JBScreen JCSG++	Jena Bioscience	CS-155
MIDASplus Screen	Molecular Dimensions	MD1-106
Morpheus Screen	Molecular Dimensions	MD1-46
Rigaku Wizard Cryo Screen 1+2	Molecular Dimensions	MD15-C12-T
Deposited data		
Structure of the N-SH2 domain of SHP2 in complex with the phosphoY627-Gab1 (613-651) peptide	This study	PDB: 9qa5
Micro-ED structure of the NSH2-CSH2 tandem domain of SHP2 in complex with the bis-phosphorylated pY627-pY659-Gab1 (613-694) peptide	This study	PDB: 9qcd
15N 1H backbone chemical shifts of unbound N-SH2 domain of Shp2	This study	BMRB: 53252
1H 15N backbone chemical shifts of 2pY Gab1 613-694	This study	BMRB: 53253
1H, 15N N-SH2 of Shp2 bound to 2pY-Gab1 617-684	This study	BMRB: 53254
1H 15N backbone chemical shifts of 2pY Gab1 617-684 bound to N-SH2 of Shp2	This study	BMRB: 53255
1H 15N backbone chemical shifts of 2pY Gab1 617-684 bound to C-SH2 domain of Shp2	This study	BMRB: 53256

(*Continued on next page*)

Please cite this article in press as: Machner et al., Mechanism of SHP2 activation by bis-Tyr-phosphorylated Gab1, Structure (2025), https://doi.org/10.1016/j.str.2025.11.018

Continued

REAGENT or RESOURCE	SOURCE	IDENTIFIER
1H, 15N Backbone chemical shifts of free C-SH2 domain of Shp2	This study	BMRB: 53257
1H, 15N backbone chemical shifts of C-SH2 domain of Shp2 bound to 2pY Gab1 617-684	This study	BMRB: 53258
Crystal structure of the tyrosine phosphatase SHP-2.	Hof et al.[4]	PDB: 2shp
Crystal structure of human tyrosine phosphatase SHP-1	Yang et al.[42]	PDB: 2b3o
Crystal structure of human protein tyrosine phosphatase SHP-1 in the open conformation	Wang et al.[34]	PDB: 3ps5
The wild-type Src homology 2 (SH2)-domain containing protein tyrosine phosphatase-2 (SHP2)	Yu et al.[53]	PDB: 4dgp
Crystal structure of the tyrosine phosphatase SHP-2 with Y279C mutation	Tan et al.[54]	PDB: 4gwf
Crystal structure of PTPN11 tandem SH2 domains in complex with a TXNIP peptide	Liu et al.[33]	PDB: 5df6
Non-receptor Protein Tyrosine Phosphatase SHP2 in Complex with Allosteric Inhibitor SHP099	Chen et al.[6]	PDB: 5ehr
Crystal structure of SHP2_SH2-CagA EPIYA_C peptide complex	Hayashi et al.[17]	PDB: 5x7b
Crystal structure of SHP2_SH2-CagA EPIYA_D peptide complex	Hayashi et al.[17]	PDB: 5x94
Structure of human SHP2 without N-SH2 domain	Pádua et al.[7]	PDB: 6cmq
Crystal Structure of Shp2 E76K GOF Mutant in the Open Conformation	LaRochelle et al.[5]	PDB: 6crf
Crystal Structure of Shp2 E76K GOF Mutant in complex with SHP099	LaRochelle et al.[5]	PDB: 6crg
Oligonucleotides		
Primers used in this study are shown in Table S1	This study	N/A
Recombinant DNA		
pET SUMO plasmid	Invitrogen	K300-01
pET42-hGab1$^{613-694}$	Gruber et al.[28]	N/A
pET28-Shp2$^{1-222}$	This study	N/A
pET21-muABL1 (138-534, F420V)-His	This study	N/A
pCDFDuet1-YopH (164-468)	John Chodera, Nicholas Levinson, Markus Seeliger	Addgene Plasmid #79749
pET200D-TOPO-Gab1	Le Goff et al.[27]	N/A
pACYC-LIC+	Cheryl Arrowsmith	Addgene Plasmid #62312
pET42a(+)	Novagen	Cat#70561
pGEX-Abl (139-543, F420V)	Welch et al.[55]	N/A
pET21d(+)	Novagen	Cat#69743
pNIC28-PTPN11	Gopalasingam[56]	N/A
Software and algorithms		
EPU-D 1.11	Thermo Fisher Scientific	N/A
NMRPipe	Delaglio et al.[57]	https://www.ibbr.umd.edu/nmrpipe/install.html
NMRViewJ	NMRFX	https://nmrfx.org/nmrfx/nmrviewj
NMRbox	Maciejewski et al.[58]	https://nmrbox.nmrhub.org/
relax	d'Auvergne et al.[59]	https://www.nmr-relax.com/
MicroCal ITC200 Analysis Software v7.20	GE Healthcare	N/A
PyMol	Schrödinger, LLC	RRID:SCR_000305
Coot	Emsley et al.[60]	RRID:SCR_014222
XDS	Kabsch[61]	RRID:SCR_015652

(*Continued on next page*)

Please cite this article in press as: Machner et al., Mechanism of SHP2 activation by bis-Tyr-phosphorylated Gab1, Structure (2025), https://doi.org/10.1016/j.str.2025.11.018

Continued

REAGENT or RESOURCE	SOURCE	IDENTIFIER
PHASER	McCoy et al.[62]	RRID:SCR_014219
PHENIX	Liebschner et al.[63]	RRID:SCR_014224
CCP4i2 suite	Potterton et al.[64]	https://www.ccp4.ac.uk/
REFMAC5	Murshudov et al.[65]	https://www.ccp4.ac.uk/html/refmac5/description
ColabFold v1.5.5: AlphaFold2 using MMseqs2	Mirdita et al.[66]	https://github.com/sokrypton/ColabFold
Origin v7.0552	OriginLab	N/A
Other		
ÄKTA pure 25 L1	Cytiva Life Sciences	Cat#29018225
HiTrap IMAC FF	Cytiva Life Sciences	Cat#17092104
HiTrap Q HP	Cytiva Life Sciences	Cat#17115401
HiLoad 16/600 Superdex 75 pg	Cytiva Life Sciences	Cat#28989333
MicroCal iTC200	Malvern Instruments	N/A
600, 800 MHz Bruker Avance III NMR spectrometers	Bruker	N/A
500 MHz Bruker DRK NMR spectrometer	Bruker	N/A
15-well hanging drop plates	Qiagen	Cat# 100234
Rotating Anode X-ray generator MicroMax007HF	Rigaku Europe SE	N/A
X-ray diffractometer goniometer UG2	Rigaku Europe SE	N/A
Cryogenic cooler Cryostream 800	Oxford Cryosystems	N/A
Hybrid photon counting detector HyPix Arc 150	Rigaku Europe SE	N/A
Ashless filter study, Grade 595	Ted Pella	47000-100
Unstretched parafilm discs	Bemis	Cat# PM-996
Quantifoil R2/1 grid (200 mesh copper)	Quantifoil	N1-C15nCu20-01
easiGLOW Plasma Cleaner	TedPella	91000S
Vitrobot Mark IV	Thermo Fisher Scientific	1086439
Glacios® Cryogenic Transmission Electron Microscope (Cryo-TEM)	Thermo Fisher Scientific	N/A
Ceta-D camera	Thermo Fisher Scientific	N/A
Falcon III EC	Thermo Fisher Scientific	N/A

EXPERIMENTAL MODEL AND STUDY PARTICIPANT DETAILS

Escherichia coli XL10 Gold (purchased from Agilent) was used for plasmid amplification. *Escherichia coli* BL21(DE3) (purchased from Thermo Fisher Scientific) was used for recombinant protein expression. Culturing conditions can be found in the method details. Primers are listed in Table S1.

METHOD DETAILS

Protein expression and purification

Preparation of Gab1 peptides

The C-terminal region of Gab1 (amino acids 613–694) was amplified from pET200D-TOPO-Gab1[27] using the primers Gab1_613-694_A_F and Gab1_613-694_A_R. The PCR product was cloned into a BsaI-linearized pACYC-LIC+ vector using seamless ligation cloning extract (SLiCE).[67] Following this, the insert was re-amplified with the primers Gab1_613-694_B_F and Gab1_613-694_B_R, digested with VspI and SalI, and ligated into the NdeI/XhoI sites of pET42a(+) (Novagen) to generate a His-tagged fusion protein. A 3C-protease cleavage site was introduced by PCR amplification of the full plasmid using Gab1_613-694_C_F and Gab1_613-694_C_R, followed by circularization using an In-Fusion HD cloning kit (Takara Bio).

The His-tagged Gab1 fusion protein was expressed in *E. coli* BL21(DE3) grown in either TB or M9 minimal medium supplemented with $^{15}NH_4Cl$ and ^{13}C-glucose for isotope labelling. Protein expression was induced at an OD600 of 1.2 by addition of IPTG at a final concentration of 0.2 mM in TB or 0.5 mM in M9, and cultures were incubated for 4 hours at 37°C. Cells were harvested by centrifugation and resuspended in lysis buffer (20 mM sodium phosphate, 500 mM NaCl, pH 7.3), containing protease inhibitors (10 μg/ml aprotinin, 5 μg/ml antipain, 0.7 μg/ml pepstatin, 0.2 mM PMSF), and disrupted by sonication (3 × 1 min, 100% power, 50% interval). Insoluble material was removed by centrifugation at 30,000 × g for 30 minutes at 4°C, repeated three times. The His-tagged protein

Please cite this article in press as: Machner et al., Mechanism of SHP2 activation by bis-Tyr-phosphorylated Gab1, Structure (2025), https://doi.org/10.1016/j.str.2025.11.018

was immobilized on Co^{2+}-charged Chelating Sepharose FF beads (GE Healthcare) and the His-tag was cleaved by incubation with recombinant GST-tagged HRV 3C protease in lysis buffer for 16 hours at 4°C.

For non-phosphorylated Gab1, the buffer was exchanged by gel filtration on a HiLoad Superdex 75 column (GE Healthcare) using 20 mM sodium citrate, 50 mM NaCl, pH 6.2. *In vitro* phosphorylation was achieved by incubating Gab1$^{613–694}$ with constitutively active Abl kinase (murine Abl1, aa 138–534, F420V)[68] (see below) in lysis buffer, supplemented with 10 mM $MgCl_2$, 4 mM ATP, and 2 mM DTT, for 5 hours at 30°C at a 1:200 (w/w) ratio. The phosphorylated protein was dialyzed overnight at 4°C against 20 mM sodium carbonate buffer, pH 9.5, containing 0.1 mM sodium vanadate and 0.1 mM sodium molybdate. Doubly, mono- and non-phosphorylated peptides were separated on a HiTrap Q HP column using a pH gradient from 11 to 4 over 40 column volumes in a multi-buffer system maintaining constant ionic strength (9.8 mM methylamine, 9.1 mM 1,2-ethanediamine, 6.4 mM 1-methylpiperazine, 13.7 mM 1,4-dimethylpiperazine, 5.8 mM Bis-Tris, 7.7 mM hydroxylamine).[69] After buffer exchange to 20 mM sodium citrate, 50 mM NaCl, pH 6.2, the purified proteins were aliquoted, shock-frozen in liquid nitrogen, and stored at −80°C. Protein purity was >95% as confirmed by SDS-PAGE, with yields of approximately 10 mg/L for non-phosphorylated and 3 mg/L for phosphorylated protein. Gab1$^{617–684}$ was generated via cyclic polymerase extension cloning (CPEC) using the primers Gab1_617-684_A_F/Gab1_617-684_A_R for amplification of the insert and Gab1_617-684_B_F/Gab1_617-684_B_R for linearization of the vector. The protein was purified using the same procedure described above. Additional Gab1 peptides (Gab1$^{667–677}$, pY^{659}-Gab1$^{655–677}$, pY^{659}-Gab1$^{655–666}$) were synthesized commercially by ProteoGenix, and pY^{627}-Gab1$^{613–651}$ and pY^{659}-Gab1$^{640-694}$ were synthesized by Davids Biotechnologie.

Expression and purification of Murine Abl kinase for peptide phosphorylation

Murine Abl kinase was co-expressed with the Yersinia tyrosine phosphatase YopH to minimize host proteome phosphorylation.[70] The Abl SH2 and kinase domains (aa 138–534, F420V) were amplified from pGEX-Abl plasmid using primers Abl_138-534_F and Abl_138-534_R and ligated into the NheI/XhoI sites of pET21d. The YopH plasmid (pCDFDuet1-YopH 164–468) and pET21-muABL1 were co-transformed into BL21(DE3) and selected on LB plates containing 100 μg/ml ampicillin and 50 μg/ml streptomycin at 37°C overnight. Cultures were scaled up from 50 ml TB starter cultures to 500-ml cultures and grown to an OD600 of 1.2 at 37°C. The cultures were cooled to 18°C before IPTG was added to a final concentration of 0.2 mM. Cultures were incubated overnight at reduced shaking speed. Cells were harvested by centrifugation at 2560 × g for 30 minutes at 4°C and stored at −80°C.

Cell pellets were resuspended in 50 mM Tris-HCl, pH 8.0, 500 mM NaCl, 5% glycerol, 25 mM imidazole supplemented with protease inhibitors (0.01 mg/ml aprotinin, 0.005 mg/ml antipain, 0.0005 mg/ml leupeptin, 0.0007 mg/ml pepstatin, 0.2 mM PMSF, 0.1 mM Na_3VO_4, 0.1 mM Na_2MoO_4, 1 mg/ml lysozyme, 1 mM DTT) and 1 mg/ml lysozyme. After sonication (3 × 1 min, 100% power, 50% interval) lysates were clarified by centrifugation at 30,000 × g for 60 minutes at 4°C. The supernatant was applied to a freshly prepared Ni^{2+}-IMAC FF column. Bound protein was eluted with a 25–275 mM imidazole gradient. Fractions containing Abl kinase were pooled, dialyzed overnight against 20 mM Tris-HCl, 25 mM NaCl, 5% glycerol, 1 mM DTT, and further purified using HiTrap Q HP anion exchange (0–350 mM NaCl gradient) and size-exclusion chromatography on Superdex 75 (50 mM Tris-HCl, 100 mM NaCl, 5% glycerol, 1 mM DTT). Purified kinase was concentrated, aliquoted, shock-frozen in liquid nitrogen, and stored at −80°C. The yield was approximately 15 mg per liter of culture.

Expression and purification of SHP2 SH2 domains

The tandem SH2 domain of SHP2 (aa 1–222) was cloned into pET28 with an N-terminal His6-TEV site using primers Shp2_1-222_F and Shp2_1-222_R. BL21(DE3) cells transformed with this plasmid were grown in TB medium with 50 μg/ml kanamycin, induced at an OD600 of ~1.0 with 0.5 mM IPTG, and incubated overnight at 18°C. Cells were harvested by centrifugation at 2560 × g for 30 minutes at 4°C and stored at −80°C.

Pellets were resuspended in IMAC binding buffer (50 mM Tris-HCl, pH 7.5, 200 mM NaCl, 20 mM imidazole, 1 mM TCEP) containing a protease inhibitor mix (0.01 mg/ml aprotinin, 0.005 mg/ml antipain, 0.0005 mg/ml leupeptin, 0.0007 mg/ml pepstatin, 0.2 mM PMSF) and lysed by sonication (3 × 1 min cycles, 100% power, 50% interval). The lysate was clarified by centrifugation at 30,000 × g for 3 hours at 4°C. The supernatant was applied to a Ni^{2+}-IMAC column, and the bound protein was eluted with 500 mM imidazole. TEV protease was added at a 1:30 molar ratio, and the mixture was dialyzed overnight against 50 mM Tris-HCl, pH 7.5, 150 mM NaCl, 1 mM TCEP. The cleaved protein was separated from His-tagged components by reverse IMAC, concentrated, and further purified by size-exclusion chromatography on a HiLoad 16/600 Superdex 75 column using one of the following buffers depending upon the subsequent experiments: 20 mM citrate buffer pH 6.0 (ITC); 20 mM bisTris/HCl, 50 mM NaCl pH 6.0 (NMR); or 50 mM Tris/HCl pH 7.5, 50 mM NaCl, 1 mM DTT (crystallisation).

The individual SH2 domains N-SH2$^{1-106}$ and C-SH2$^{102-220}$ were subcloned into a pET-SUMO plasmid (Invitrogen K300-01) by CPEC. Inserts were generated using the primer pairs Shp2_1-106_F/Shp2_1-106_R and Shp2_102-220_F / Shp2_102-220_R, respectively. The vector was linearised by PCR using the primer pair pET-SUMO_lin_F/pET-SUMO_lin_R. The individual domains were expressed as N-His$_6$-SUMO-fusion proteins, purified by Co^{2+} affinity chromatography (chelating Sepharose FF loaded with cobalt (II) sulphate heptahydrate) using 500 mM imidazole as elution buffer, and cleaved overnight at 4°C using SUMO-protease in an 1:50 (w/w) ratio. The dialysed cleavage product was applied to a second IMAC column to remove the tag and the protease. The flow-through was concentrated and further purified using size-exclusion chromatography (HiLoad 16/600 Superdex 75 pg) with the same process-specific buffers as described for the tandem domain. This method was also used for the SH2-dead variants[17] N-SH2^{dead}, C-SH2^{dead}, SHP2$^{1-222}$-C-SH2^{dead} and SHP2$^{1-222}$-N-SH2^{dead} generated by QuikChange mutagenesis using the primers

Please cite this article in press as: Machner et al., Mechanism of SHP2 activation by bis-Tyr-phosphorylated Gab1, Structure (2025), https://doi.org/10.1016/j.str.2025.11.018

Shp2_R32A/Shp2_H53A (N-SH2^{dead} and SHP2$^{1-222}$-N-SH2^{dead}) or Shp2_R138A/Shp2_H169A (C-SH2^{dead} and SHP2$^{1-222}$-C-SH2^{dead}).

Isothermal titration calorimetry

ITC experiments were performed at 25°C using a MicroCal iTC200 instrument. Proteins and peptides were dialyzed against 10 mM citrate buffer, pH 6.0, containing 1 mM TCEP. Protein concentrations were determined spectroscopically. Although in principle a two-binding site model could apply for the interaction between the tandem SH2 domain and doubly phosphorylated Gab1$^{613-694}$, the high affinity results in a very steep isotherm with very few experimental points at the inflection. We therefore applied a single binding model to avoid overfitting of this curve, resulting in an apparent K_d. Control measurements were subtracted from experimental data using Origin 7.0 software.

X-ray crystallography of N-SH2: pY^{627}-Gab1 complex

N-SH2$^{1-106}$ (20 mg/ml) crystallised in the presence of a 1.5 molar excess of pY^{627}-Gab1$^{613-651}$ in 15-well hanging drop plates. Tetragonal bipyramidal crystals appeared in 25% PEG3350, 0.2 M NaCl, 0.1 M BisTris pH 5.5 within a few days.

Prior to data collection, a single crystal was flash frozen in liquid nitrogen, with 10% ethylene glycol added as cryoprotectant. Diffraction data were collected in-house at 100 K with Cu Kα radiation (λ=1.5418 Å) using a hybrid photon counting detector (HyPix-Arc 150°, Rigaku/MSC, Tokyo, Japan) mounted on a rotating anode generator (Micromax 007, Rigaku/MSC, Tokyo, Japan). X-ray diffraction data to 2.08 Å were indexed and integrated using XDS.[61] The structure was solved by molecular replacement in PHASER[62] using the deposited structure of N-SH2$^{1-106}$:Gab1$^{621-633}$ (PDB code 4qsy, Gogl and Remenyi, unpublished) as search model with the Gab1 peptide removed. The structure was completed by iterative model building in COOT[60] and refinement using PHENIX.[63] All structure figures were generated using PyMOL (The PyMOL Molecular Graphics System, Version 3.0 Schrödinger, LLC).

3D electron diffraction of SHP2 tandem SH2: pYpY-Gab1

Crystals of SHP2$^{1-222}$ (25 mg/ml) in complex with pY^{627}pY^{659}-Gab1$^{617-684}$ (7.7 mg/ml) were obtained by hanging-drop vapour diffusion at 12°C in 15-well plates. Thin needle-like crystals appeared within a week in 29% PEG 3350 and 0.1 M Tris/HCl pH 8.8. SDS-PAGE of dissolved crystals confirmed the presence of both proteins (25 kDa SHP2$^{1-222}$ and 8 kDa Gab1 peptide). Although weak diffraction to 3.5 Å was observed with in-house X-ray sources, macroscopic crystals exhibited considerable disorder with multiple lattices, prompting the use of 3D electron diffraction (3D-ED/MicroED), a continuous crystal rotation diffraction acquisition scheme.[71] Additional details of the procedures are provided elsewhere.[31]

For grid preparation, 3.5 μl of the crystal suspension was applied to the carbon side of glow-discharged Quantifoil® R2/1 (200 mesh) holey carbon grids, while an equal volume of 1:1 diluted crystallisation buffer was pipetted to the copper side. Grids were blotted for 25 s at 4°C and 95% humidity (Vitrobot® Mark IV, Thermo Fisher Scientific) from the copper site using (Ø55/20mm, Grade 595) and similarly cut parafilm from the carbon side and vitrified by plunge-freezing into ethane.

Diffraction data were collected on a 200 keV Thermo Scientific Glacios cryo-TEM. Crystals were identified in TEM mode using the Falcon III EC detector, while diffraction patterns were recorded on a Ceta-D camera. Data were acquired from two crystals in perpendicular orientations across a tilt range of −70° to +70°, with the centre measured from -30° to 30° and wider angles measured in smaller wedges of 20° to 40° range, each. The microscope was adjusted in parallel beam nano-probe mode with an exposure area limited by 50 μm C2 aperture (i.e., a beam size of 1.7 μm). To minimise radiation damage, new crystal areas (>2 μm apart) were used for each wedge (20°–40°). The electron flux was ~0.046 $e^-/Å^2/s$, with a cumulative fluence of 3–4 $e^-/Å^2$ per dataset.

Data processing with XDS[61] yielded a 3.2 Å dataset with 89% completeness in space group $P2_12_12_1$, containing one complex per asymmetric unit. Phases were obtained by molecular replacement with PHASER (CCP4i2 suite)[62,64]], using the SHP2$^{1-222}$–phospho-TXNIP peptide structure (PDB 5df6)[33] as search model, after removal of peptides and separation of N-SH2 (residues 1–104) and C-SH2 (residues 108–220) domains. Restrained jelly body refinement was performed with REFMAC5[65] using electron scattering factors. Model building in COOT[60] was guided by the N-SH2$^{1-106}$:pY^{627}-Gab1$^{613-651}$ structure and the C-SH2$^{108-220}$ domain from the TXNIP complex. Final rounds of refinement were performed using PHENIX[63] including riding H-atoms and using electron scattering factors.

After refinement, additional Coulomb potential density was detected at the C-SH2 surface. Manual modelling in COOT showed good agreement with a Gab1 fragment predicted by AlphaFold2 for SHP2$^{1-593}$:Gab1$^{611-694}$. The final model comprises SHP2 residues 6–221 and two Gab1 fragments (residues 624–634 and 653–672).

NMR spectroscopy

^{15}N- and ^{13}C-labeled proteins were expressed in M9 medium containing $^{15}NH_4Cl$ and ^{13}C-glucose. NMR experiments, including 2D ^{15}N-^{1}H HSQC and TROSY as well as 3D HNCA, HNCACB, HNCO, and HN(CA)CO for $^{13}C^{15}N$ N-SH2 and $^{13}C^{15}N$-C-SH2, were performed on a Bruker Avance III 800 MHz spectrometer equipped with a CP-TCI cryoprobe at 25°C. Measurements were made using a 500-750 μM protein sample in 20 mM BisTris/HCl, 50 mM NaCl, pH 6.0, 10% D_2O (v/v) with sodium trimethylsilylpropanesulfonate (DSS) as chemical shift standard. For the SH2 tandem domain, the ^{15}N TROSY spectrum was superimposed on those of the N- and

Please cite this article in press as: Machner et al., Mechanism of SHP2 activation by bis-Tyr-phosphorylated Gab1, Structure (2025), https://doi.org/10.1016/j.str.2025.11.018

C-SH2 domains, and cross-peaks in uncrowded regions of the spectrum were used for identification of isolated residues. All spectra were processed using NMRPipe[57] and analysed in NMRView.[72] Chemical shift perturbations were determined using formula:

$$\mathrm{CSP} = \sqrt{\frac{\Delta^2\delta(^1\mathrm{H})+\frac{1}{25}\Delta^2\delta(^{15}\mathrm{N})}{2}}$$

Chemical shift indices[73] for Gab1 peptides were calculated through comparison of the observed chemical shifts with a calculated chemical shift dataset for the same protein in the denatured state, taking into account phosphorylation of the tyrosine residues[74]: $\mathrm{CSI} = (\mathrm{C}\alpha\text{-}\mathrm{C}\beta)_{\mathrm{exp}} - (\mathrm{C}\alpha\text{-}\mathrm{C}\beta)_{\mathrm{calc}}$

^{1}H-^{15}N steady-state heteronuclear NOE (hNOE) experiments were measured in proton-saturated and unsaturated states. Longitudinal relaxation times (T_1), whose inverse provides the relaxation rate R_1 (= $1/T_1$), were measured by inverting the magnetisation from the z to -z-axis by a 180° pulse followed by varying delay times of 0 ms, 50 ms, 100 ms, 150 ms, 200 ms, 300 ms, 500 ms, 750 ms, 1000 ms and 1500 ms. The magnetisation was then flipped to the xy-axis by a 90° pulse for detection. To measure the transversal relaxation (T_2), the magnetisation was excited by a 90° pulse, and a series of measurements with varying spin-lock periods of 0 ms, 8 ms, 16 ms, 32 ms, 48 ms, 64 ms, 80 ms, 96 ms, 112 ms, 160 ms were recorded. The intensity of each peak in a series of experiments was determined by NMRview or PINT.[75]

Relaxation measurements (T_1, T_2, hNOE) were collected additionally on an Avance III 600 MHz and a Bruker DRX 500 MHz spectrometer. Order parameters S^2 were calculated from R_1, R_2 and hNOE measured at 800 MHz, 600 MHz and 500 MHz using the Lipari-Szabo model-free analysis[76] processed in the NMR Box environment[58] with the program *relax*,[59] which finds the best local model of motion by an optimized global rotational diffusion tensor.

Modelling of Gab1-bound SHP2

The pYpY-Gab1 complex with SHP2 in the proposed active state (Figure 7A) was modelled using PyMOL, starting from the coordinates of SHP2 ΔN-SH2 (pdb 6cmq, chain C). The C-SH2 domain of the pYpY-Gab1-bound tandem domain solved here (pdb 9qcd) was superimposed on that of 6cmq (chain C) as shown in Figure S11G. The tandem domain was then manually adjusted as a rigid body to juxtapose conserved interface residues to the catalytic domain (Figure S8) derived from the active state of SHP1 (3ps5). Residues missing from the modelled SHP2 structure, as well as those linking the Gab1 N- and C-terminal peptides, were built using COOT, avoiding clashes with the folded domains.

Starting from the autoinhibited SHP2 conformation (pdb 2shp), the pYpY-Gab1 peptide bound to the inactive state (Figure 7B) was modelled by separate superposition of the N-SH2:N-terminal Gab1 peptide and the C-SH2:C-terminal peptide upon 2shp. As for the putative active state, the intervening linker was built using COOT.

QUANTIFICATION AND STATISTICAL ANALYSIS

X-ray crystallography data collection, Micro-ED data collection and refinement statistics are summarized in Table 1. Statistical tests and number of replicates are described in the figure legends.

Structure, Volume *34*

Supplemental Information

Mechanism of SHP2 activation by bis-Tyr-phosphorylated Gab1

Lisa Machner, Alaa Shaikhqasem, Tobias Gruber, Farzad Hamdi, Constanze Breithaupt, Judith Kniest, Felix Wiebe, Marc Lewitzky, Christoph Parthier, Fotis L. Kyrilis, Jochen Balbach, Panagiotis L. Kastritis, Stephan M. Feller, and Milton T. Stubbs

Supplemental information

Mechanism of SHP2 activation by bis-Tyr-phosphorylated Gab1

Lisa Machner, Alaa Shaikhqasem, Tobias Gruber, Farzad Hamdi, Constanze Breithaupt, Judith Kniest, Felix Wiebe, Marc Lewitzky, Christoph Parthier, Fotis L. Kyrilis, Jochen Balbach, Panagiotis L. Kastritis, Stephan M. Feller and Milton T. Stubbs

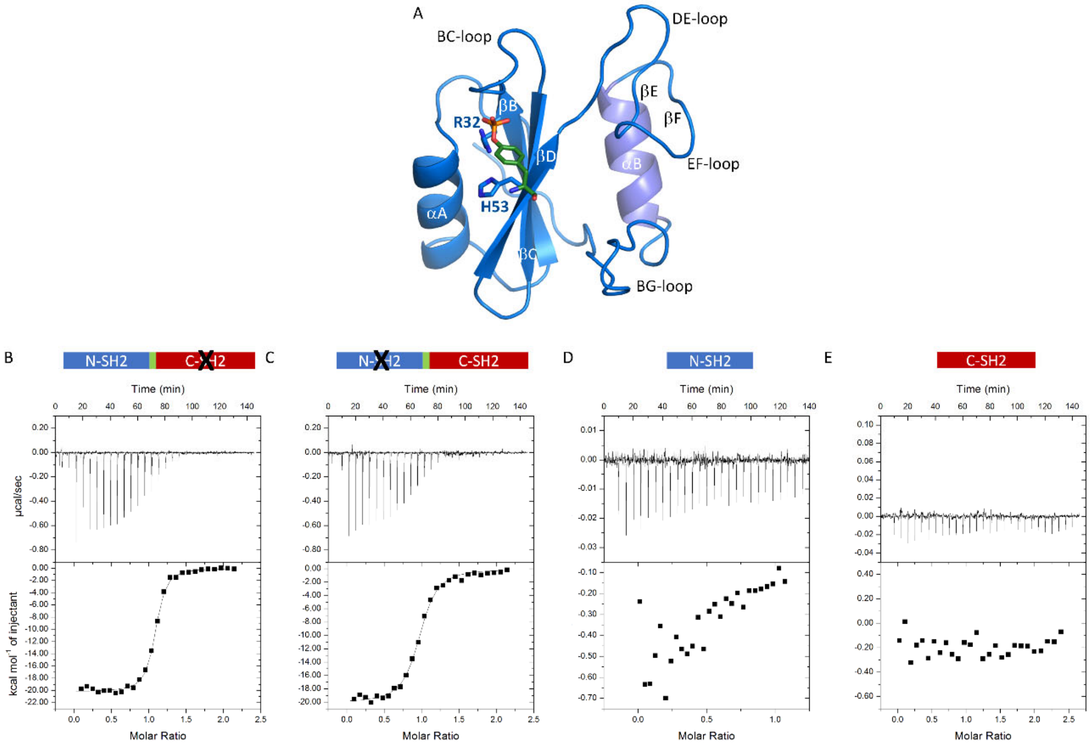

	Shp2$^{1-222}$-C-SH2 dead : Gab1$^{613-94}$	Shp2$^{1-222}$-N-SH2 dead : Gab1$^{613-94}$	N-SH2$^{1-106}$: Gab1$^{640-694}$	C-SH2$^{102-220}$: Gab1$^{613-651}$
N	1.04 ± 0.04	1.01 ± 0.07		
K_D [nM]	128 ± 14	293 ± 56		
- ΔS · T	11111 ± 394	11081 ± 506		
ΔH	-20517 ± 345	-19970 ± 540		
ΔG	-9339 ± 52	-8922 ± 119		

Figure S1. Single site binding interactions of Gab1 – SHP2 SH2 domains analysed by ITC, related to Figure 1. (A) Residues R^{32} and H^{53} (shown in stick representation) in the N-SH2 domain, corresponding to residues R^{138} and H^{169} in the C-SH2 domain, constitute the binding site for phosphopeptide pY phosphate groups. Their mutation to alanine yields N-SH2^{dead} (R^{32}A/H^{53}A) and C-SH2^{dead} (R^{138}A/H^{169}A) [1]. **(B, C)** Deleting one of the two phosphotyrosine binding sites in the tandem domain (SHP2$^{1-222}$-C-SH2^{dead} (R^{138}A/H^{169}A) and SHP2$^{1-222}$-N-SH2^{dead} (R^{32}A/H^{53}A)) results in reduced affinity compared to the wild type tandem domain (**Figure 2A**), yet higher than for the isolated domains (**Figure 2B, C**). **(D, E)** The isolated N-SH2 domain SHP2$^{1-106}$ shows no measurable enthalpy change in the presence of the singly phosphorylated pY^{659}-Gab1$^{640-694}$ peptide, nor does the C-SH2 domain SHP2$^{102-220}$ in the presence of pY^{627}-Gab1$^{613-651}$.

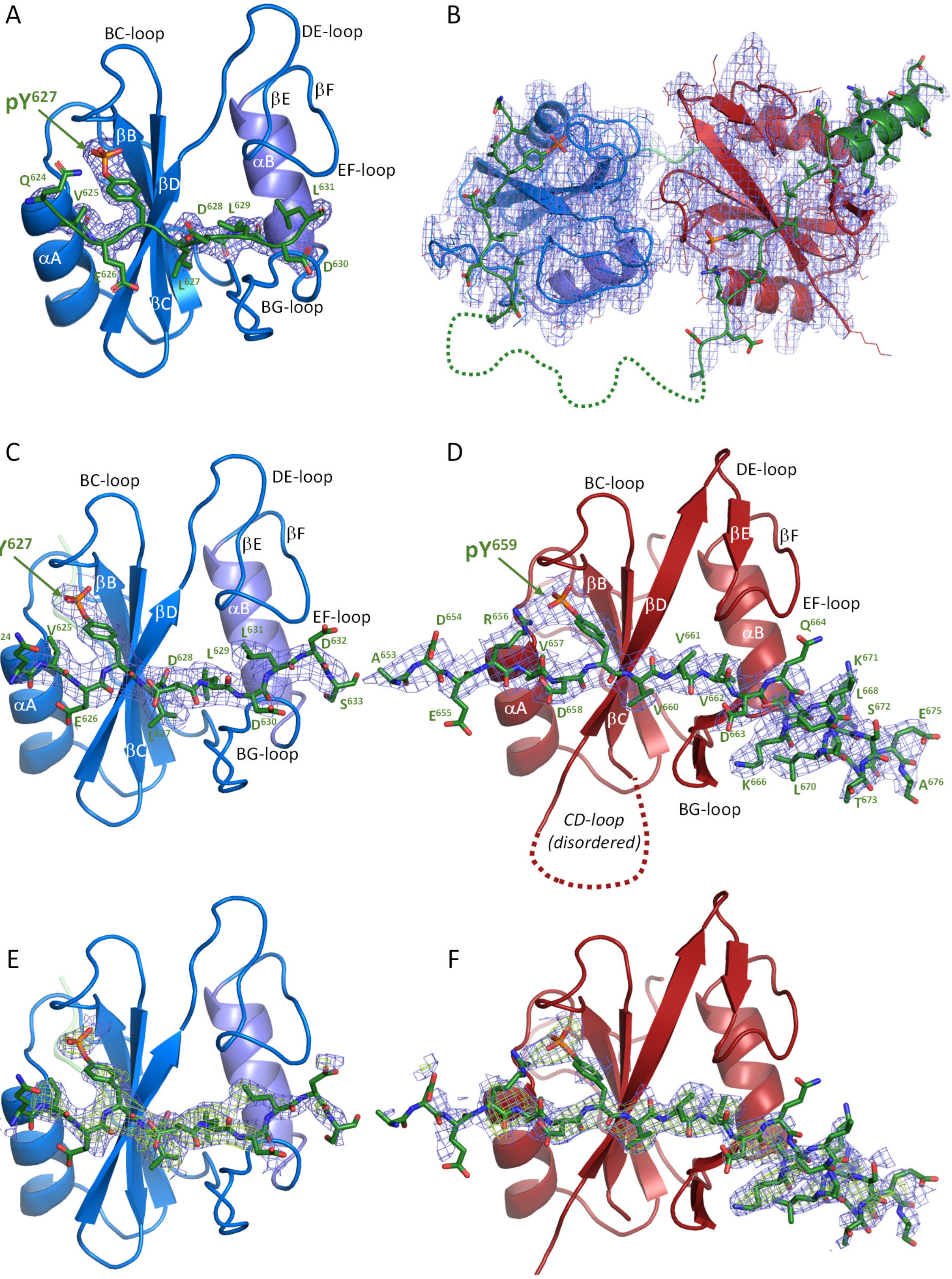

Figure S2. Experimental crystallographic densities for phosphotyrosine peptide binding to SHP2 SH2 domains, related to Figure 3. **(A)** 2Fo-Fc electron density for the pY^{627}-Gab1$^{613\text{-}651}$ peptide (green sticks) bound to the isolated N-SH2 domain contoured at 1σ. **(B)** Overall 2Fo-Fc Coulomb potential density (1σ) for the N-SH2-C-SH2-tandem SHP2$^{1\text{-}222}$ construct (blue/red) in complex with pY^{627}pY^{659}-Gab1$^{617\text{-}684}$ (green) determined by electron crystallography. **(C, D)** Experimental 2Fo-Fc Coulomb potential density (1σ) for the pY^{627}pY^{659}-Gab1$^{617\text{-}684}$ peptide bound to the SH2 domains in the tandem construct, with each domain oriented corresponding to **(A)**. **(E,F)** Omit maps corresponding to **(C)** and **(D)** calculated after structure refinement in the absence of the peptides (blue: 2Fo-Fc contoured at 0.9 σ; green: Fo-Fc at 2.5 σ).

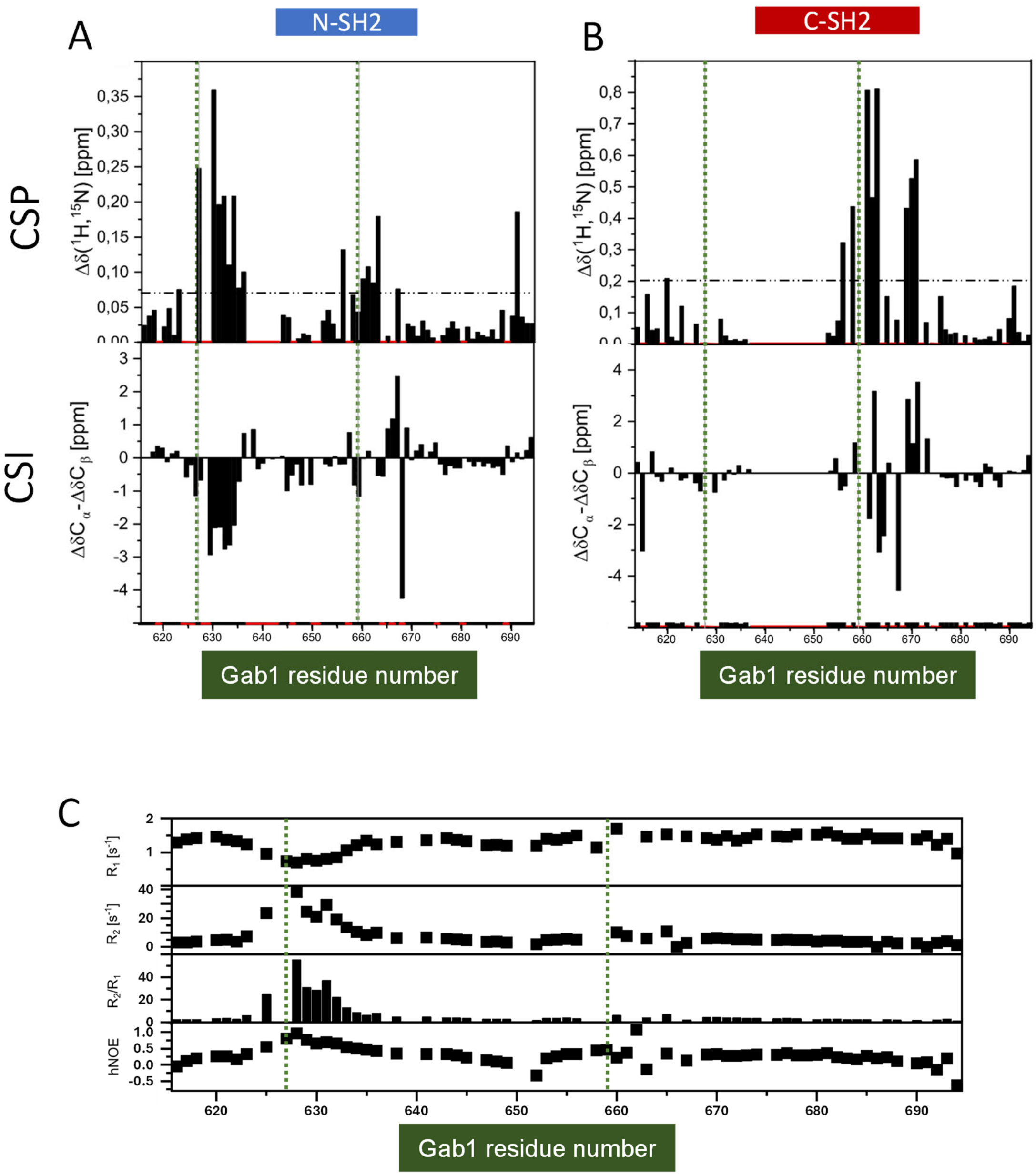

Figure S3. Interaction of ^{15}N-pY^{627}pY^{659}-Gab1$^{613\text{-}694}$ with unlabelled N-SH2$^{1\text{-}106}$ and C-SH2$^{106\text{-}220}$ domains in solution, related to Figure 4. (A) Chemical shift perturbations (CSPs) in ppm upon titration of ^{15}N,^{13}C-pY^{627}pY^{659}-Gab1$^{613\text{-}694}$ to N-SH2 indicate that residues adjacent to both pY^{627} and pY^{659} (indicated by green dotted lines) bind to the N-SH2 domain. Chemical shift indices (CSIs), where negative values indicate extended and positive values helical backbone conformations, indicate an extended conformation for Gab1 residues 630-635. **(B)** Upon titration of the labelled peptide to C-SH2, CSPs indicate residues 655-671 adjacent to pY^{659} bind the C-SH2 domain, a sequence that is considerably longer than typical (canonical) SH2-domain binding regions. CSIs for residues 661-665 correspond to an extended conformation, whereas those for amino acids 669-673 are indicative of an α-helix. **(C)** ^{15}N NMR relaxation rates (R_1 and R_2) and hNOE of ^{15}N-pYpY-Gab1$^{613\text{-}694}$ in complex with the N-SH2 domain measured at 600 MHz proton frequency. Increased R_2/R_1 ratios and hNOE values compared to the parameters for free ^{15}N-pYpY-Gab1$^{613\text{-}694}$ [2] indicate conformational restriction around pY^{627} upon N-SH2 binding. Secondary structure elements of the domains are coloured according to **Figure 1**.

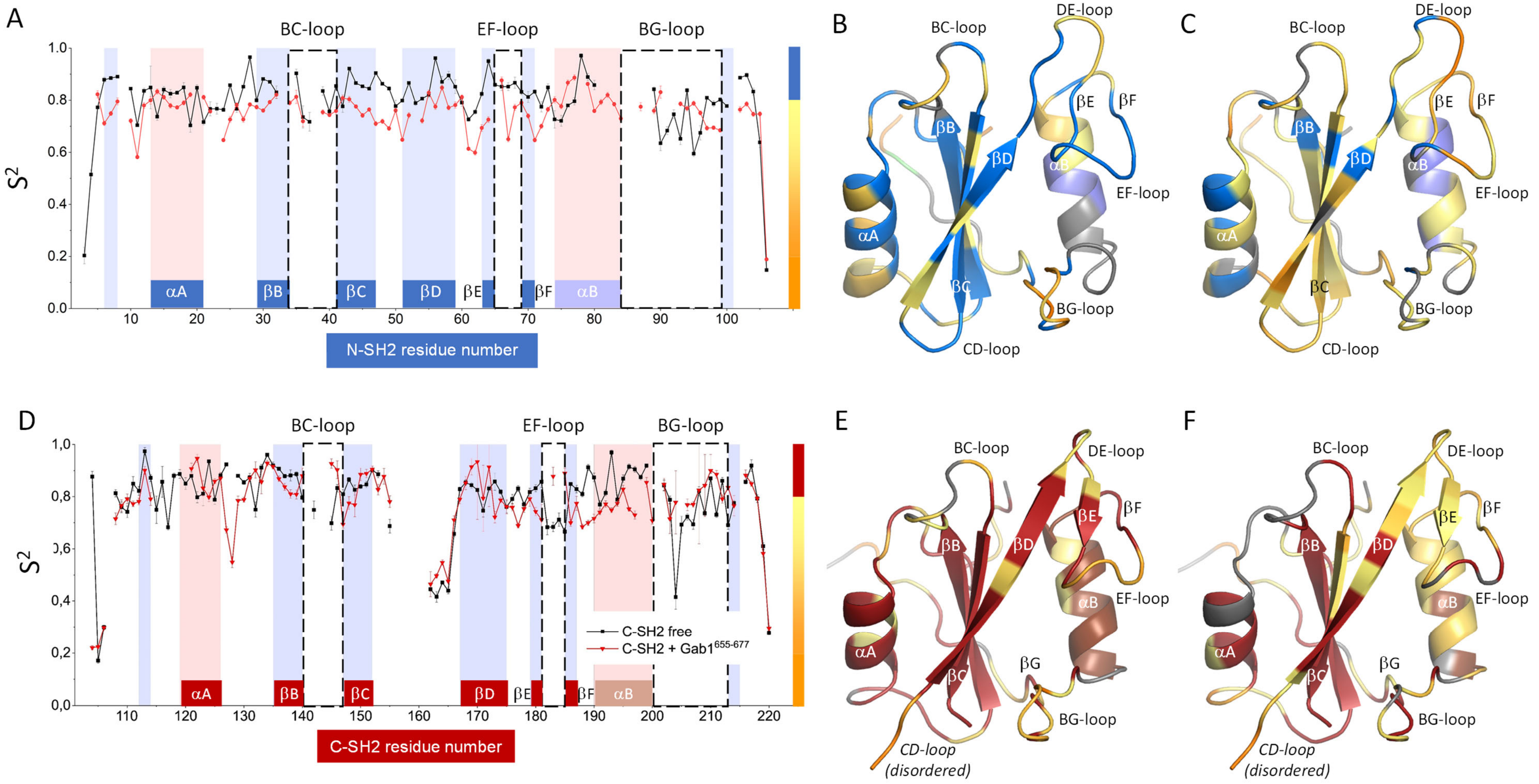

Figure S4. NMR order parameter changes upon binding of unlabelled pY-Gab1 peptides to individual ^{15}N-labelled SHP2 SH2 domains in solution, related to Figure 4. (A) Per residue Lipari-Szabo order parameter S^2 for ^{15}N-N-SH2$^{1\text{-}106}$ for the free domain (black) and the pY-Gab1$^{613\text{-}651}$ bound state (red) derived from data presented in **Figure S5 (A, B)** using the program package *relax*. **(B, C)** Order parameters for the **(B)** free and **(C)** peptide-bound N-SH2 domains mapped to the crystal structure. **(D-F)** Corresponding plots for the free ^{15}N-C-SH2$^{102\text{-}220}$ domain (black) and the pY-Gab1$^{655\text{-}677}$ bound state (red) derived from data in **Figure S5 (C)** and **(D).** Missing S^2 values in **(A)** and **(D)** are due to non-assigned residues and are coloured grey in the structural mappings. Secondary structure elements of the domains are coloured according to **Figure 1**.

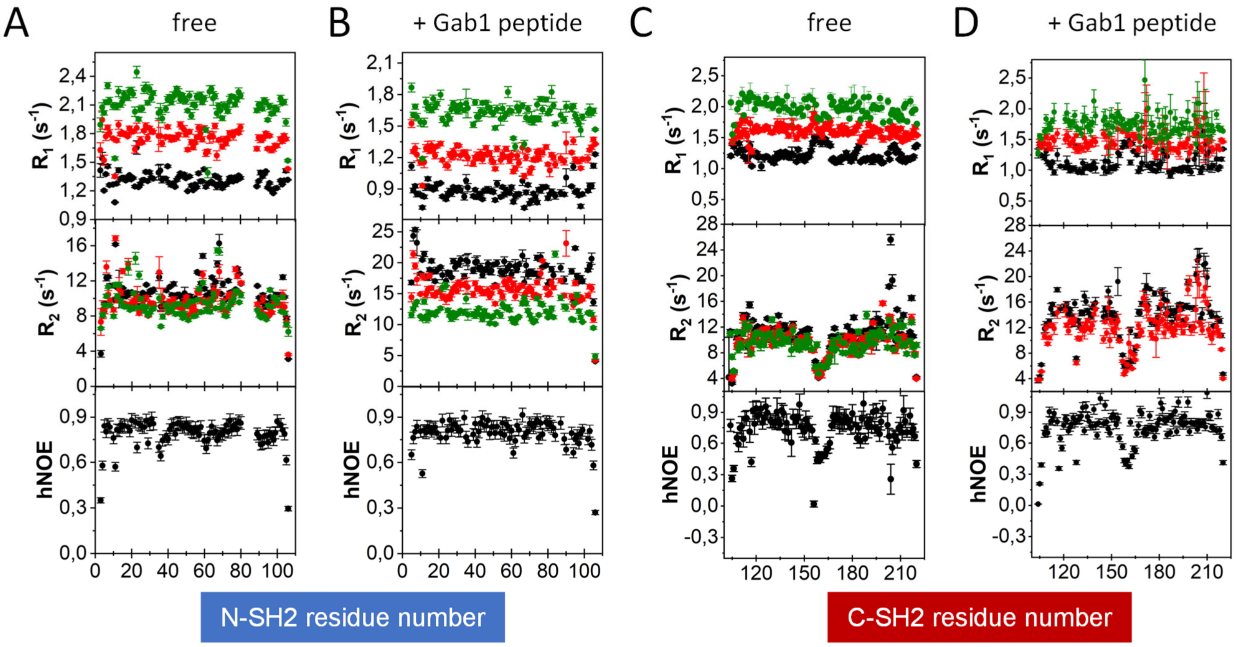

Figure S5. Solution NMR relaxation data for ^{15}N-N-SH2$^{1\text{-}106}$ and ^{15}N-C-SH2$^{106\text{-}220}$ domains in the absence and presence of their respective pY-Gab1 peptides, related to Figure 4. (A, B) ^{15}N R_1 and R_2 rates and hNOE values of ^{15}N-N-SH2$^{1\text{-}106}$ measured at 800 MHz (black), 600 MHz (red) and 500 MHz (green) in the **(A)** free and **(B)** pY-Gab1$^{613\text{-}651}$ bound states. The latter shows additional global chemical exchange contributions to the R2 rates compared to the free state. (**C, D**) Corresponding data for ^{15}N-C-SH2$^{106\text{-}220}$ in the **(C)** free and **(D)** pY-Gab1$^{655\text{-}677}$ bound states. Error bars come from line shape fitting in PINT[3]. These data were used for calculating S^2 values shown in **Figure S4**.

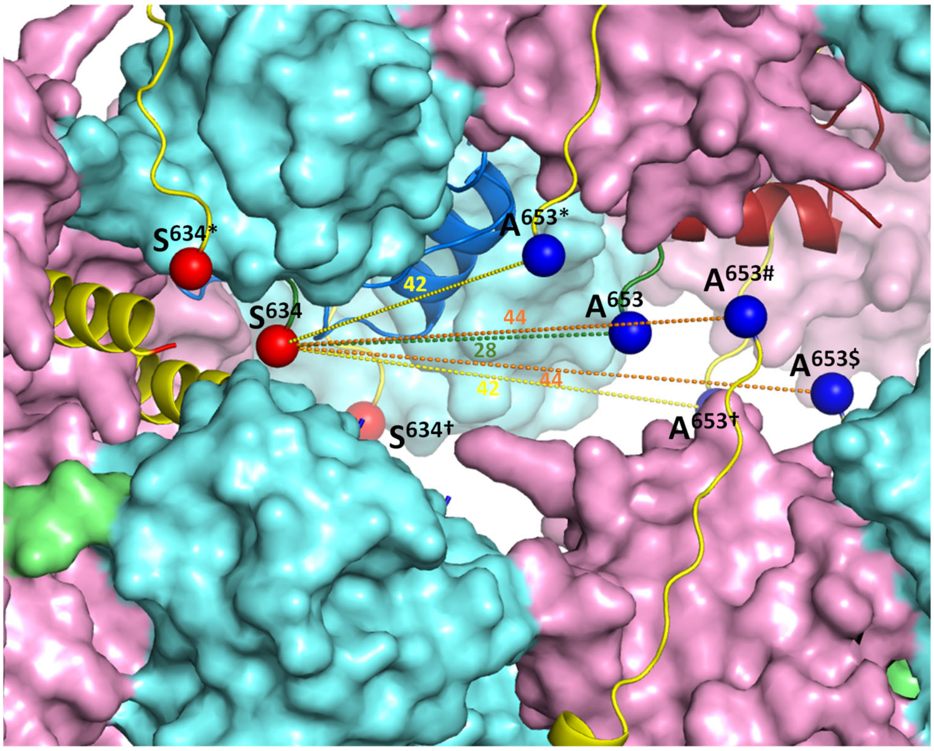

Figure S6. The intermolecular space in the tandem domain crystals would allow alternative connectivities of the disordered 18 residue Gab1 linker peptide G^{635}-V^{652}, related to Figure 6. The shortest of these (28 Å, dark green, measured from S^{634} Cα (red) to A^{653} Cα (blue)) corresponds to both pY-peptide segments binding to a single tandem N-SH2-C-SH2 domain (cartoon representation, colours as in **Figure 1**), i.e. a 1:1 stoichiometry. Distances linking S^{634} and A^{653} of symmetry-related molecules (yellow and orange, Cα atoms labelled*†#$, N-SH2 and C-SH2 domains as cyan and violet surfaces respectively) are longer (42 Å and 44 Å); these connectivities would imply a single pYpY-Gab1 peptide bridging two tandem domains, possibly leading to higher order SHP2 assemblies.

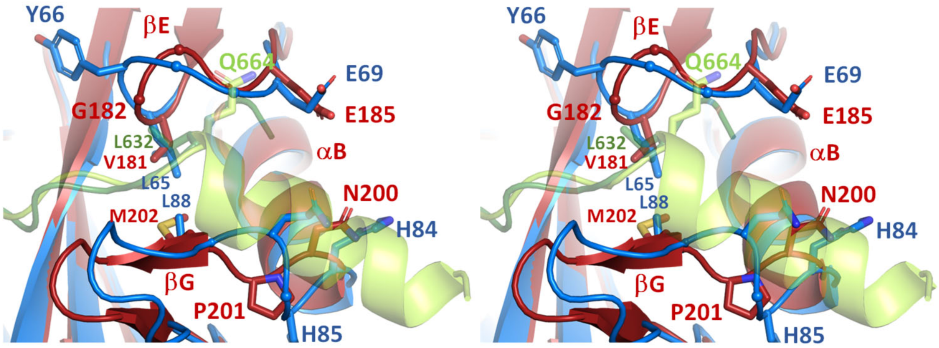

Figure S7. Specificity determinants for peptide binding to SHP2 N- and C-SH2 domains, related to Figure 3. Superposition of peptide ligand pY+x binding sites in stereo representation, peptides shown as transparent green cartoons. The C-SH2 EF-loop adopts a different mainchain conformation as a result of the sequence ^{181}VGGGE^{185} (^{65}LYGGE^{69} in the N-SH2 domain), which could lead to relaxation of the specificity for hydrophobic residues at position pY+5 (Gab1 side chains L^{632} (dark green) vs. Q^{664} (light green) respectively). The presence of the proline-containing C-SH2 sequence ^{200}NPM^{202} (corresponding to the five-residue N-SH2 segment ^{84}HHGQL^{88}) in the BG-loop results in a more open peptide binding site that facilitates accommodation of the extended C-terminal helix in Gab1. These sequences are conserved in SHP2 N- and C-SH2 domains respectively (**Figure S8**).

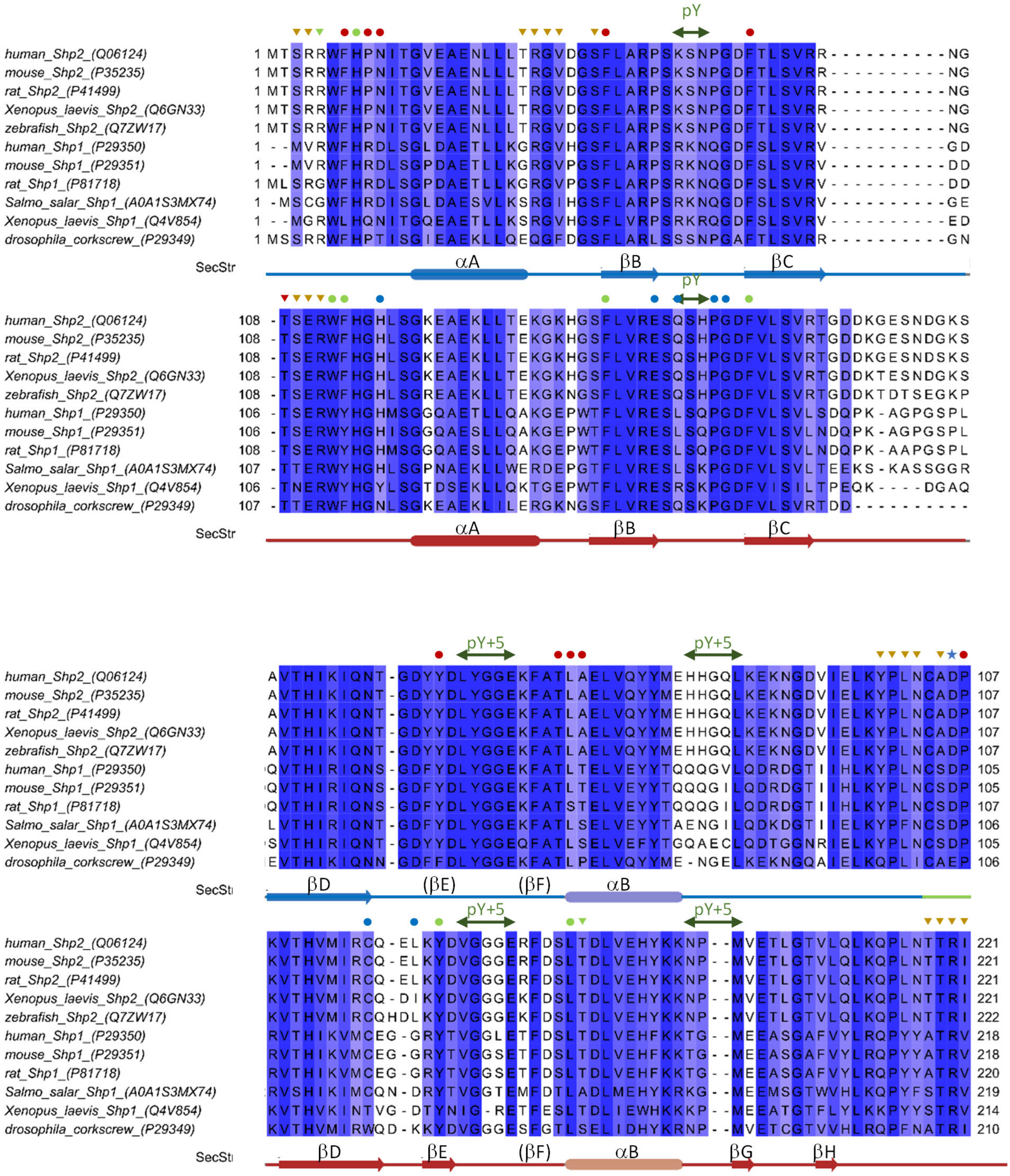

Figure S8. Multiple sequence alignment of N-SH2 and C-SH2 domains from SHP2 and SHP1, related to Figure 6. Residues corresponding to the N-SH2:C-SH2 interface found in the pYpY-Gab1 bound tandem domain structure described here are depicted by circles coloured according to their binding partners (blue: N-SH2; red: C-SH2; light green: interdomain linker). SH2 sequences involved in binding to Gab1 peptide pY and pY+5 residues are indicated with a double headed dark green arrow. Additional residues involved in the N-SH2:C-SH2 interface found in the SHP1 open state[4] are marked with coloured triangles; yellow triangles indicate residues that interact with the SHP1 catalytic domain.

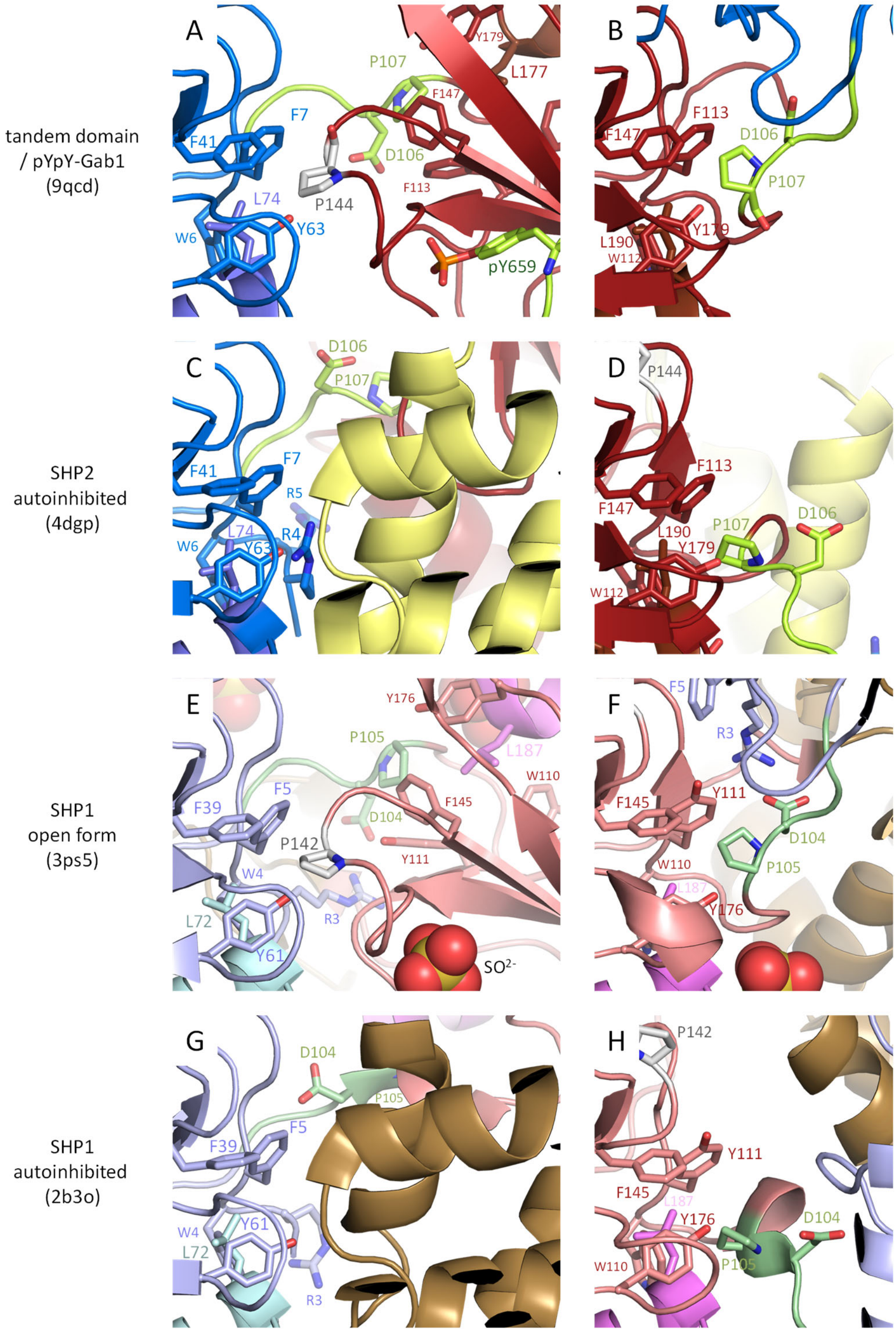

Figure S9. A hydrophobic pocket in the SHP2 N-SH2 domain, occupied in the present structure by P^{144}, is structurally conserved in SHP2/SHP1 N- and C-SH2 domains, related to Figure 6. (A) In the present structure (PDB 9qcd), C-SH2 P^{144} (white sticks) nestles in a hydrophobic pocket formed by N-SH2 residues W^{6}, F^{7}, F^{41}, Y^{63} and L^{74} (blue sticks). Superpositioning the C-SH2 domain on the N-SH2 domain **(B)** reveals a corresponding pocket composed of W^{112}, F^{113}, F^{147}, Y^{179} and L^{190} (red sticks) occupied by P^{107} of the interdomain linker (green). **(C)** In the autoinhibited conformation of wild type SHP2 (PDB code 4dgp),[5] access to the N-SH2 pocket is restricted by residues of the catalytic domain (yellow) and partially occupied by the side chain of R^{4}, whereas the corresponding pocket in the C-SH2 domain **(D)** is free. PDB coordinates 4dgp[5] are displayed as the construct used for 2shp[6] carried a mutation F^{41}L, although the environment is the same. **(E)** In the open form of SHP1 (3ps5)[4], P^{142} occupies the corresponding N-SH2 hydrophobic pocket, R^{3} approaches interdomain linker D^{104} (green) and P^{105} enters the C-SH2 pocket **(F)**. In autoinhibited SHP1 (2b3o)[7], the N-SH2 pocket **(G)** is blocked by the catalytic domain (brown), and the C-SH2 pocket **(H)** is unoccupied.

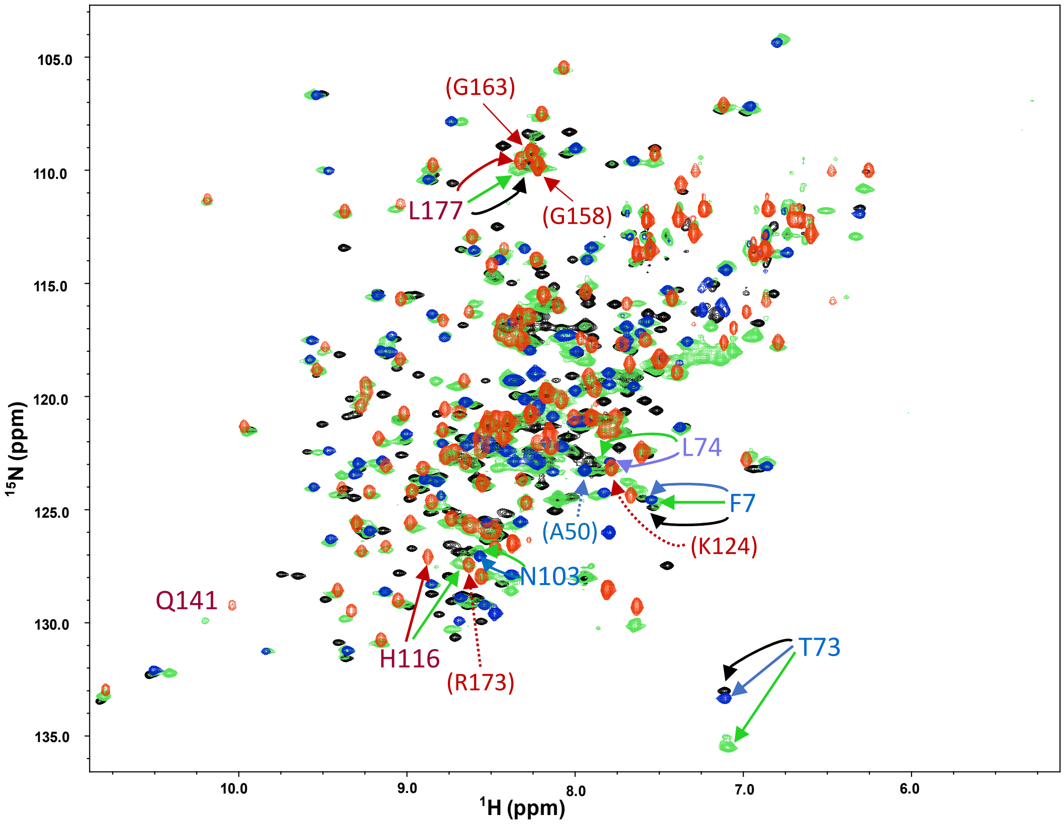

Figure S10. TROSY spectra of SHP2 domains, related to Figure 6. Superposition of the ^{15}N-TROSY spectra of the SHP2 tandem domain SHP2$^{1\text{-}222}$ in the free (black) and pY^{627}pY^{659}-Gab1$^{613\text{-}694}$ bound state (green) together with those of the bis-phosphorylated Gab1$^{613\text{-}694}$ bound ^{15}N-N-SH2$^{1\text{-}106}$ (blue) and ^{15}N-C-SH2$^{102\text{-}220}$ (red) domains. Residue numbers correspond to those shown in **Figure 6J**; residues in parentheses correspond to selected cross-peaks that do not shift. Note that the cross-peak for T^{73} is identical in the free tandem domain (black) and the pY^{627}pY^{659}-Gab1$^{613\text{-}694}$ bound N-SH2 (blue) spectra, indicating the observed shift in the tandem domain resonances upon peptide binding (green) is due to local environmental changes in the N-SH2-C-SH2 tandem domain.

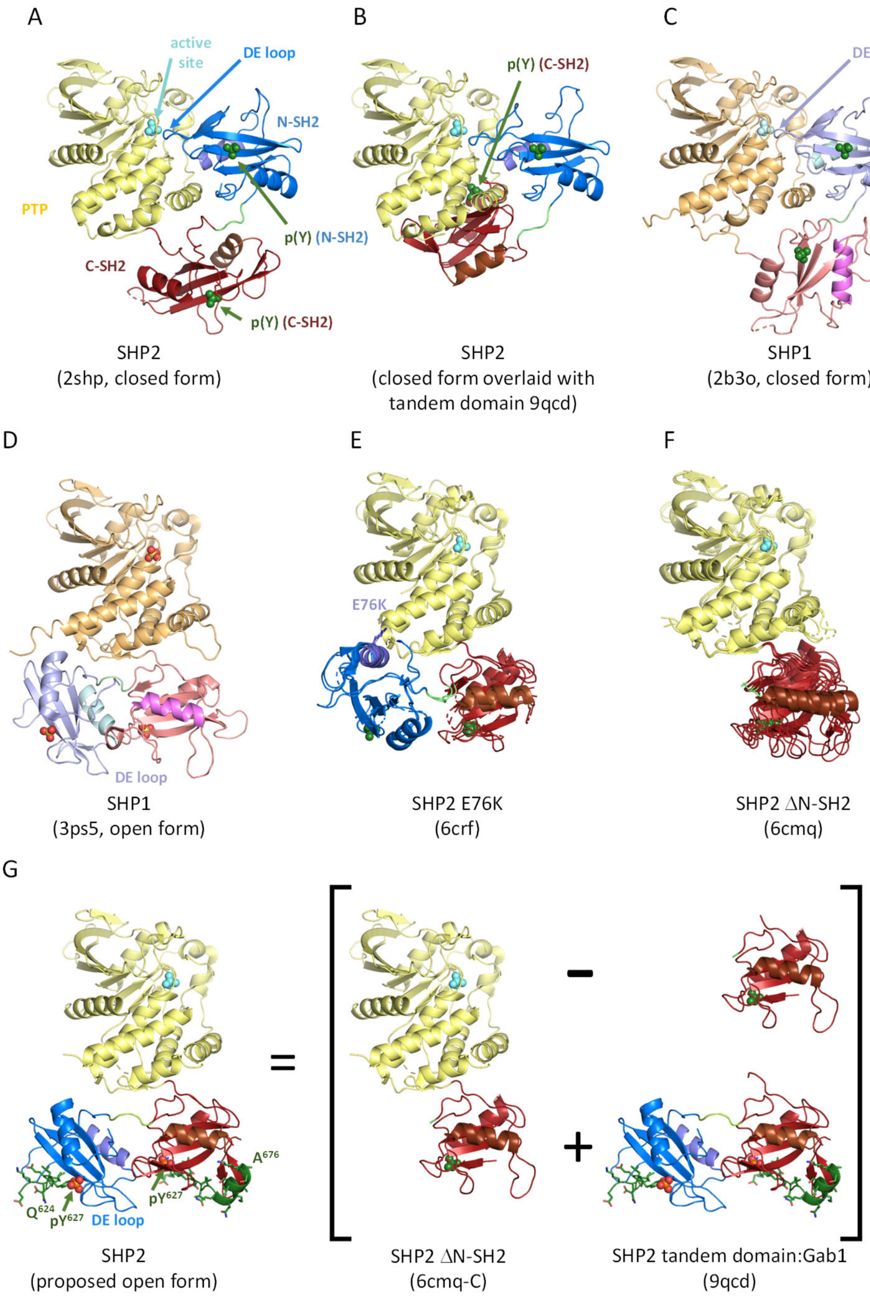

SHP2
(2shp, closed form)

SHP2
(closed form overlaid with tandem domain 9qcd)

SHP1
(2b3o, closed form)

SHP1
(3ps5, open form)

SHP2 E76K
(6crf)

SHP2 ΔN-SH2
(6cmq)

SHP2
(proposed open form)

SHP2 ΔN-SH2
(6cmq-C)

SHP2 tandem domain:Gab1
(9qcd)

Figure S11. Domain architectures of SHP1 and SHP2 constructs, related to Figure 7; orientation of the PTP domain and colours as in Figure 1. (A) Structure of autoinhibited SHP2 (pdb code 2shp)[6]. **(B)** The pYpY-Gab1-bound N-SH2:C-SH2 domain interaction seen here is incompatible with the closed conformation, as superposition of the N-SH2 domains results in clashes of the C-SH2 domain with the PTP-domain. **(C)** Structure of autoinhibited SHP1 (2b3o)[7]; colours as in **Figure 6H**. The SHP1 N-SH2 domain is in an equivalent position to that in SHP2 (**A**), but the C-SH2 is rotated. **(D)** SHP1 crystallised in an open form (3ps5)[4] in the presence of detergent and ammonium sulphate; three sulphate ions from the crystallisation buffer occupy the PTP active site and the phosphotyrosine binding sites of the two SH2 domains (spheres). **(E)** In the absence of inhibitor, the constitutively active oncogenic variant SHP2^{E76K} adopts an open conformation (6crf)[8]. In both molecules of the asymmetric unit, the C-SH2 domain exhibits the same orientation relative to the PTP domain as seen in the SHP1 open form (**D**). **(F)** Crystals of SHP2$^{\Delta N\text{-}SH2}$ lacking the N-SH2 domain (6cmq)[9] also show the C-SH2 domain in an equivalent position in all four molecules of the asymmetric unit. **(G)** Superposition of the C-SH2 domain of the SHP2 tandem domain in complex with pY^{627}-pY^{659}-Gab1$^{622\text{-}672}$ on that of SHP2$^{\Delta N\text{-}SH2}$ (6cmq chain C)[9] yields an open domain architecture corresponding to that of SHP1 (**D**).

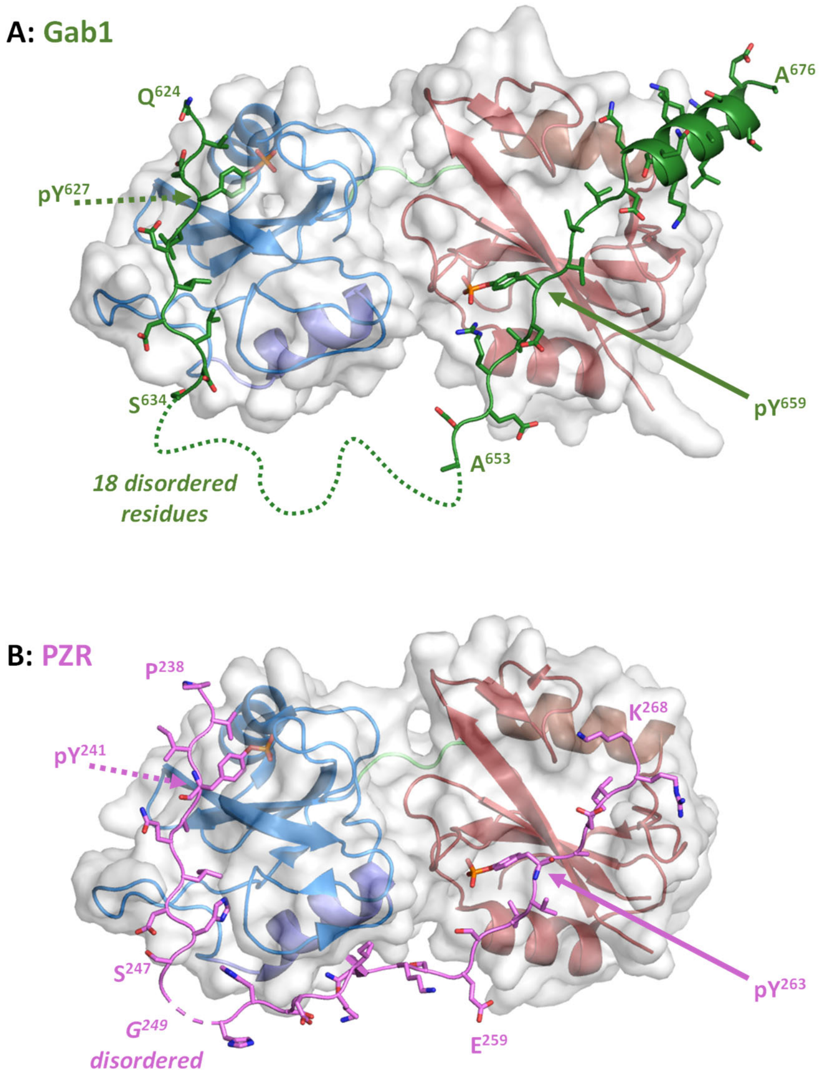

Figure S12. Two structures of SHP2 tandem domains co-crystallized with bis-tyrosine-phosphorylated activator peptides exhibit a similar compact arrangement, with a common N-SH2:C-SH2 interface, related to Figure 6. (A) $pY^{627}pY^{659}$-Gab1$^{617\text{-}684}$ (dark green, this study, pdb code 9qcd) interacts with the tandem domain though pY^{627}-Gab1$^{624\text{-}634}$ binding to the N-SH2 domain in an extended (canonical) conformation and pY^{659}-Gab1$^{653\text{-}676}$ binding to the C-SH2 domain in a novel extended/helical conformation. 18 of the 31 inter-pY linker peptide residues are disordered in the crystal. **(B)** During the final revision of this manuscript, a crystal structure was released (pdb code 9mq5)[10] of the SHP2 tandem domain in complex with the bis-phosphorylated activator peptide $pY^{241}pY^{263}$-PZR$^{237\text{-}269}$ (pink, derived from the C-terminal region of myelin protein zero-like protein 1). Both pY-PZR segments bind their respective SH2 domains in a canonical conformation, with no helix formation. Only one residue (G249) of the 21 residue inter-pY linker is disordered. As the peptide sequence, binding mode and crystal form are completely different in the two structures, it seems likely that the compact arrangement reflects a common architecture related to the activated state.

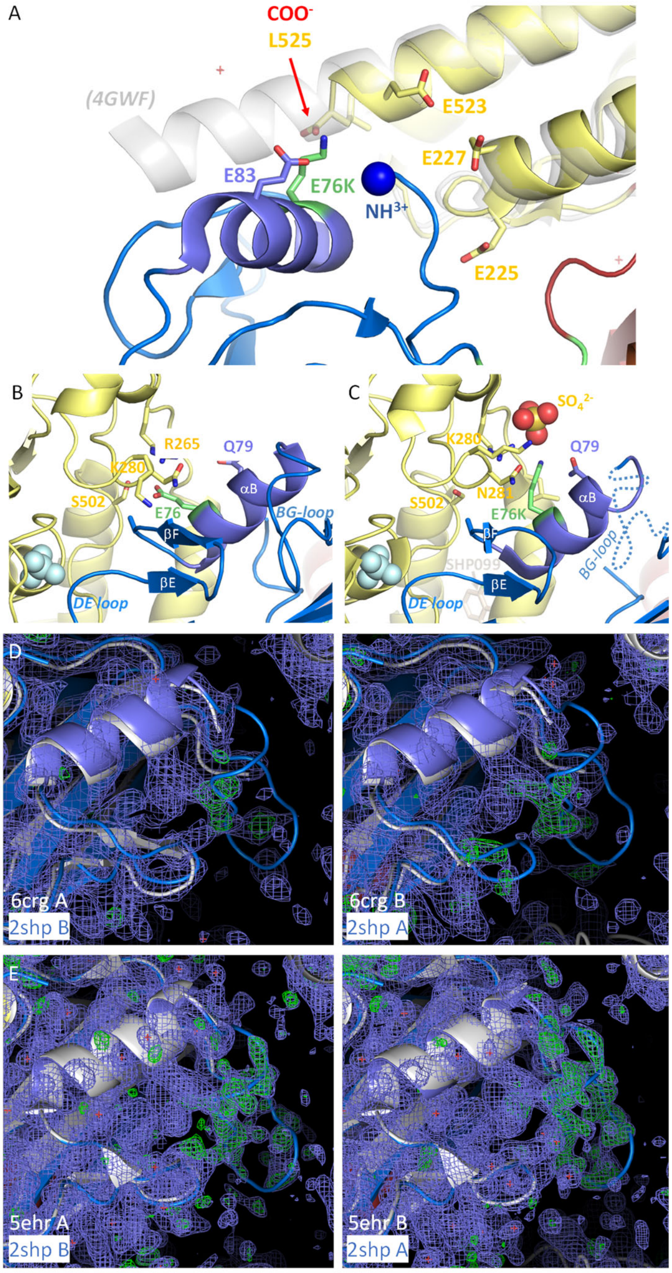

Figure S13. Environment of E76K in the oncogenic SHP2 mutant, related to Figure 7. (A) In the SHP2 E76K mutant structure (6crf)[8], the position of the N-SH2 domain is perturbed due to the charge reversal of the E76K side chain, which is found together with the polypeptide amino terminus in the neighbourhood of a negatively charged patch formed by Glu83, Glu225, Glu227 and Glu523, as well as the carboxy terminus Leu525 of the SHP2 SHP2 E76K$^{1\text{-}525}$ construct used for crystallisation. The latter interaction is not available in full length SHP2; moreover, structures of SHP2 mutants using SHP2 variant$^{1\text{-}539}$ constructs[S1] demonstrate that the C-terminus extends as an α-helix (transparent cartoon, pdb code 4gwf) that would clash sterically with the N-SH2 domain in this position. **(B)** Neighbourhood of E76 in autoinhibited SHP2$^{\text{wt}}$ (2shp)[6], where all residues shown are defined. **(C)** In the presence of the allosteric inhibitor SHP099 (6crg)[8], SHP2$^{\text{E76K}}$ adopts the closed (autoinhibited) state, but the positively charged E76K side chain appears to be incompatible with this position, recruiting a sulphate ion from the crystallisation buffer. Residues H^{85}-D^{94} are not present in the pdb deposition 6crg; calculating 2Fo-Fc (blue, 1σ) and Fo-Fc (green, 3σ) omit densities **(D)** from the deposited coordinates and structure factors confirm that this region is disordered in both monomers of the asymmetric unit. In contrast, clear density is present for these residues in SHP2$^{\text{wt}}$ in complex with SHP099 (pdb code 5ehr)[11] in the same crystal form. We therefore conclude that the observed disorder arises from the oncogenic mutant SHP2$^{\text{E76K}}$ adopting the autoinhibited state through binding of SHP099, indicating in turn that the mutation destabilizes the closed state.

Table S1. Primer sequences, related to **STAR*Methods.**

Primer Name	**Sequence**
Gab1_613-694_A_F [2]	TGGTTCCGCGTGGTAGTAGCAGCCCTATGATCAAG
Gab1_613-694_A_R [2]	GCCGCAAGCTTCGTCATCATTTCACACTCTTCGCTG
Gab1_613-694_B_F [2]	CGGATTAATATGGGCAGCAGCCATC
Gab1_613-694_B_R [2]	CTCGTCGACTCATTTCACACTCTTCG
Gab1_613-694_C_F [2]	CTGGAAGTTCTGTTCCAGGGGCCCAGCAGCCCTATGATCAAG
Gab1_613-694_C_R [2]	CCTGGAACAGAACTTCCAGGCCGCTGCTGTGATG
Gab1_617-684_A_F	GTTCTGTTCCAGGGGCCCATCAAGCCCAAAGGAGACA
Gab1_617-684_A_R	GTGGTGGTGCTCGACTCATGTGGACTGTCTCCCATC
Gab1_617-684_B_F	TGAGTCGAGCACCACCAC
Gab1_617-684_B_R	GGGCCCCTGGAACAGAAC
Abl_138-534_F	CGGGCTAGCGTCAACAGCCTGGAGAAAC
Abl_138-534_R	GCGCTCGAGCGTGCCTCGTTTC
Shp2_1-222_F [2]	ATATCATATGCACCATCATCATCATCATTC
Shp2_1-222_R	TTATTGGATCCTCATTAGTTAATGCGCG
Shp2_1-106_F	AGAGAACAGATTGGTGGTATGACCAGCCGTCGCT
Shp2_1-106_R	CCGAATAAATACCTAAGCTTTTATTAATCTGCGCAGTTCAGCGG
Shp2_102-220_F	AGAGAACAGATTGGTGGTCTGAACTGCGCAGATCCGA
Shp2_102-220_R	CCGAATAAATACCTAAGCTTTTATTAGCGCGTGGTATTCAGC
pET-SUMO_lin_F	TAATAAAAGCTTAGGTATTTATTCGG
pET-SUMO_lin_R	ACCACCAATCTGTTCTCT
Shp2_R32A	GATGGCAGTTTTCTGGCGGCTCCGAGCAAATCTAATCC
Shp2_H53A	TCGCAATGGCGCAGTTACCGCCATTAAAATCCAGAACACG
Shp2_ R138A	ATGGCTCTTTTCTGGTGGCTGAAAGTCAGAGCCACC
Shp2_H169A	ATGGCAAAAGCAAAGTTACCGCTGTGATGATTCGTTGTCAGG

SUPPLEMENTARY REFERENCES

S1. Qiu, W., Wang, X., Romanov, V., Hutchinson, A., Lin, A., Ruzanov, M., Battaile, K.P., Pai, E.F., Neel, B.G., and Chirgadze, N.Y. (2014). Structural insights into Noonan/LEOPARD syndrome-related mutants of protein-tyrosine phosphatase SHP2 (PTPN11). BMC structural biology *14,* 10. 10.1186/1472-6807-14-10.

1. Hayashi, T., Senda, M., Suzuki, N., Nishikawa, H., Ben, C., Tang, C., Nagase, L., Inoue, K., Senda, T., and Hatakeyama, M. (2017). Differential Mechanisms for SHP2 Binding and Activation Are Exploited by Geographically Distinct Helicobacter pylori CagA Oncoproteins. Cell reports 20, 2876–2890. 10.1016/j.celrep.2017.08.080.
2. Gruber, T., Lewitzky, M., Machner, L., Weininger, U., Feller, S.M., and Balbach, J. (2022). Macromolecular Crowding Induces a Binding Competent Transient Structure in Intrinsically Disordered Gab1. Journal of molecular biology 434, 167407. 10.1016/j.jmb.2021.167407.
3. Niklasson, M., Otten, R., Ahlner, A., Andresen, C., Schlagnitweit, J., Petzold, K., and Lundström, P. (2017). Comprehensive analysis of NMR data using advanced line shape fitting. Journal of biomolecular NMR *69,* 93–99. 10.1007/s10858-017-0141-6.
4. Wang, W., Liu, L., Song, X., Mo, Y., Komma, C., Bellamy, H.D., Zhao, Z.J., and Zhou, G.W. (2011). Crystal structure of human protein tyrosine phosphatase SHP-1 in the open conformation. Journal of cellular biochemistry *112,* 2062–2071. 10.1002/jcb.23125.
5. Yu, Z.-H., Xu, J., Walls, C.D., Chen, L., Zhang, S., Zhang, R., Wu, L., Wang, L., Liu, S., and Zhang, Z.-Y. (2013). Structural and mechanistic insights into LEOPARD syndrome-associated SHP2 mutations. The Journal of biological chemistry *288,* 10472–10482. 10.1074/jbc.M113.450023.
6. Hof, P., Pluskey, S., Dhe-Paganon, S., Eck, M.J., and Shoelson, S.E. (1998). Crystal structure of the tyrosine phosphatase SHP-2. Cell *92,* 441–450. 10.1016/s0092-8674(00)80938-1.
7. Yang, J., Liu, L., He, D., Song, X., Liang, X., Zhao, Z.J., and Zhou, G.W. (2003). Crystal structure of human protein-tyrosine phosphatase SHP-1. The Journal of biological chemistry *278,* 6516–6520. 10.1074/jbc.M210430200.
8. LaRochelle, J.R., Fodor, M., Vemulapalli, V., Mohseni, M., Wang, P., Stams, T., LaMarche, M.J., Chopra, R., Acker, M.G., and Blacklow, S.C. (2018). Structural reorganization of SHP2 by oncogenic mutations and implications for oncoprotein resistance to allosteric inhibition. Nature communications *9,* 4508. 10.1038/s41467-018-06823-9.
9. Pádua, R.A.P., Sun, Y., Marko, I., Pitsawong, W., Stiller, J.B., Otten, R., and Kern, D. (2018). Mechanism of activating mutations and allosteric drug inhibition of the phosphatase SHP2. Nature communications *9,* 4507. 10.1038/s41467-018-06814-w.
10. Perla, S., Stiegler, A.L., Yi, J.-S., Enyenihi, L., Zhang, L., Riaz, M., An, E., Qyang, Y., Boggon, T.J., and Bennett, A.M. (2025). SHP2 genetic variants in NSML-associated RASopathies disrupt the PZR-IRX transcription factor signaling axis. Proceedings of the National Academy of Sciences of the United States of America *122,* e2503631122. 10.1073/pnas.2503631122.
11. Chen, Y.-N.P., LaMarche, M.J., Chan, H.M., Fekkes, P., Garcia-Fortanet, J., Acker, M.G., Antonakos, B., Chen, C.H.-T., Chen, Z., and Cooke, V.G., et al. (2016). Allosteric inhibition of SHP2 phosphatase inhibits cancers driven by receptor tyrosine kinases. Nature *535,* 148–152. 10.1038/nature186213. Wang, W., Liu, L., Song, X., Mo, Y., Komma, C., Bellamy, H.D., Zhao, Z.J., and Zhou, G.W. (2011). Crystal structure of human protein tyrosine phosphatase SHP-1 in the open conformation. Journal of cellular biochemistry 112, 2062–2071. 10.1002/jcb.23125.